

Global parametric solutions of scalar transport

D.R. Lester ^{a,*}, M. Rudman ^b, G. Metcalfe ^a, H.M. Blackburn ^c

^a CSIRO Materials Science and Engineering, P.O. Box 56, Highett, Vic. 3190, Australia

^b CSIRO Mathematical and Information Sciences, Locked Bag 33, Clayton South, Vic. 3169, Australia

^c Department of Mechanical and Aerospace Engineering, Monash University, Clayton, Vic. 3800, Australia

Received 8 February 2007; received in revised form 21 August 2007; accepted 8 October 2007

Available online 30 October 2007

Abstract

Passive scalar transport involves complex interactions between advection and diffusion, where the global transport rate depends upon scalar diffusivity and the values of the (possibly large) set of parameters controlling the advective flow. Although computation of a single solution of the advection–diffusion equation (ADE) is simple, in general it is prohibitively expensive to compute the parametric variation of solutions over the full parameter space \mathcal{Q} , even though this is crucial for, e.g. optimization, parameter estimation, and elucidating the global structure of transport. By decomposing the flows within \mathcal{Q} so as to exploit symmetries, we derive a spectral method that solves the ADE over \mathcal{Q} three orders of magnitude faster than other methods of similar accuracy. Solutions are expressed in terms of the exponentially decaying natural periodic patterns of the ADE, sometimes called “strange eigenmodes”. We apply the method to the experimentally realisable rotated arc mixer chaotic flow, both to establish numerical properties and to calculate the fine-scale structure of the global solution space for transport in this chaotic flow. Over 10^5 solutions within \mathcal{Q} are resolved, and spatial pattern locking, a symmetry breaking transition to disordered spatial patterns, and fractally distributed optima in transport rate are observed. The method exhibits exponential convergence, and efficiency increases with resolution of \mathcal{Q} .
Crown Copyright © 2007 Published by Elsevier Inc. All rights reserved.

PACS: 47.52.+j; 47.54.–r; 47.20.Ky; 47.51.+a

Keywords: Chaotic advection–diffusion; Strange eigenmodes; Parametric variation; Numerical methods

1. Introduction

Dispersion of a passive scalar via simultaneous advection and diffusion is important to a wide array of physical phenomena, spanning fields from epidemiology to geophysics and length scales from the molecular to the celestial [32]. Interaction between advection and diffusion is complex, especially in the case where the advective flow field generates Lagrangian chaos [10]. Besides the balance between advective and diffusive timescales, how scalar transport evolves depends crucially on the set of parameters controlling the advective flow topology. In systems with

* Corresponding author.

E-mail address: daniel.lester@csiro.au (D.R. Lester).

parameters a natural question is what qualitative changes occur as these parameters are varied? Fundamental to operations such as process optimization, parameter identification and the study of the global structure of transport, is resolution of scalar transport over the (possibly large) multi-dimensional flow control parameter space \mathcal{Q} .

For example, micromixing devices possess a number of tunable design and operating parameters which require optimization. Previous studies only considered a handful of parameter combinations [22,30,26] within \mathcal{Q} ; however standard optimization routines can fail as transport rates can be fractally distributed [17], and so robust global optimization requires high resolution global exploration of \mathcal{Q} . Using traditional methods, repeat solution of the governing advection–diffusion equation (ADE) for very many points within \mathcal{Q} renders such operations prohibitively expensive.

In this paper we present a novel spectral method which facilitates rapid (up to 6000 times faster than the finite volume method) exploration of \mathcal{Q} by exploiting symmetries present in the set of underlying advective flows within \mathcal{Q} . The ADE is solved in terms of natural persistent patterns – sometimes called “strange eigenmodes” [19] – eigenmodes of the advection–diffusion operator, and the eigenvalues give the associated scalar transport rates. Efficiency of the method arises from the ability to rapidly approximate this operator for any point in \mathcal{Q} from a subset of fundamental operators, and subsequently solve the associated eigenproblem. While the solution method is general, we demonstrate its numerical properties and illustrate the unexpected richness of the ADE’s solution space using the chaotic rotated arc mixing (RAM) flow [21].

1.1. Motivation

The transport of a diffusing passive scalar ϕ in a velocity field $\hat{\mathbf{v}}$ is described by the advection–diffusion equation (ADE)

$$\frac{\partial \phi}{\partial t} + \hat{\mathbf{v}}(\chi) \cdot \nabla \phi = \frac{1}{Pe} \nabla^2 \phi \quad (1)$$

with appropriate boundary and initial conditions. (We consider homogeneous boundary conditions throughout but extend to inhomogeneous in [Appendix A](#)). We write $\hat{\mathbf{v}}$ as a function of χ to emphasize that the velocity field depends on a set of parameters χ specific to the particular problem and flow field under study. For example, for Taylor–Couette flow χ contains the inner and outer cylinder radii and rotation rates, the aspect ratio, and fluid rheology; for an industrial process, χ may be the set of design, operating, and rheology parameters; or, for a geophysical flow χ may contain radiative or solutal forcing parameters. The Peclet number ($Pe = L V_0/D$ with D the scalar diffusivity, L the system’s length scale, and V_0 the flow velocity scale) is the ratio of timescales for diffusion and advection. The full parameter space of the ADE is $\mathcal{Q} : \chi \times Pe$, over which the qualitative and quantitative characteristics of ADE solutions may vary significantly.

Having global parametric solutions of (1) over \mathcal{Q} would be useful to many objectives, such as optimization, solving inverse problems, or insight into the fundamental structure of scalar transport. For example, if ϕ is temperature in a heat exchanger, what flow maximises heat transfer at a particular Pe ? If ϕ is species concentration, which point in \mathcal{Q} gives fastest dispersion; conversely what structured distributions of ϕ are possible for a particular flow? Alternately, if the evolution of ϕ is observed, which point in \mathcal{Q} produced that evolution? Moreover, a parameter set χ_0 can have some error, and it may be desirable to know how robust a solution is, i.e. what, if any, transport changes are expected in the neighbourhood of χ_0 ? However, calculating global parametric solutions for (1) has been limited by the computational expense of numerical solution to an appropriate resolution over \mathcal{Q} . Numerical methods typically require a different computation for each point in parameter space to a sufficiently long time to observe the final spatial pattern and calculate its decay rate. Previous studies of the ADE have either used model flows, e.g. sine flow, that greatly simplify matrices for the projected advection operator [5,33] or, when specifically aimed at optimization, have calculated solutions at only $\mathcal{O}(10^1)$ points in \mathcal{Q} [15,3,28,26,22]. [Fig. 3](#) will show a solution space resolved with $\mathcal{O}(10^5)$ points.

1.2. Background

Recent work has firmly established that “strange eigenmodes” – sets of naturally persistent spatial patterns (NPPs) with decaying amplitudes – are fundamental solutions of the ADE. First reported by Pierrehumbert

[25] from simulations of a diffusive tracer in a time-aperiodic velocity field, NPPs were first observed in the experiments of Rothstein et al. [27] on arrays of magnetically driven vortices. Subsequently Liu and Haller [19] gave NPPs mathematical rigor by proving their existence for unsteady, but not necessarily periodic, velocity fields as a consequence of the ADE having, under reasonable conditions, an inertial manifold to which the scalar distribution tends. For time-periodic velocity fields the NPPs are Floquet modes of the advection–diffusion operator $\mathcal{L}_2[\varphi] = -\hat{\mathbf{v}} \cdot \nabla \varphi + \frac{1}{Pe} \nabla^2 \varphi$, and ϕ can be expressed as a finite sum of NPPs $\varphi_k(\mathbf{x}, t)$ and an arbitrarily small fast decaying non-eigenmode contribution $\mathcal{O}(e^{-\rho t})$:

$$\phi(\mathbf{x}, t) = \sum_{k=0}^K \alpha_k \varphi_k(\mathbf{x}, t) e^{\lambda_k t} + \mathcal{O}(e^{-\rho t}). \quad (2)$$

In (2) α_k are the weights arising from initial conditions, and λ_k are eigenvalues of \mathcal{L}_2 , the real part of which order the modes such that $Re(\lambda_0)$ corresponds to the smallest eigenvalue. For $Pe > 0$ the λ_k have negative real parts, and because for most flows there is reasonable separation between the real parts of adjacent λ_k , all but the shortest time dynamics require only the leading few eigenmodes. For sufficiently long times only the most slowly decaying term present in the initial condition persists¹:

$$\phi(\mathbf{x}, t) \rightarrow \phi_\infty(\mathbf{x}, t) = \alpha_0 \varphi_0(\mathbf{x}, t) e^{\lambda_0 t}, \quad (3)$$

and the long-time transport rate is characterised solely by λ_0 .

As passive scalar dynamics are governed by (2), we will solve for the dominant few φ_k and λ_k by first approximating the periodic velocity field $\hat{\mathbf{v}}$ by a piecewise steady flow \mathbf{v} , and then expanding \mathcal{L}_2 in spectral basis functions of the diffusion operator \mathcal{L}_1 appropriate to the domain. Because the \mathcal{L}_1 basis functions are independent of \mathbf{v} , χ , and Pe , they do not change over \mathcal{Q} . Whilst an approximation to general flows, the piecewise steady decomposition is exact for the class of reoriented duct flows [29] and other composite flows, such as the blinking-vortex, the tendril-whorl, etc. [23]. Composing the velocity from a set of steady flows allows full use of any symmetries in the problem, and we call this a *composite spectral method*, whose novelty does not come from being a spectral method, but from the ability to efficiently calculate global parametric solutions of the transport Eq. (1) and its generalizations, which should be a powerful tool for understanding and controlling scalar transport.

1.3. Outline

The paper is organised as follows. Section 1 briefly reviews the nature and properties of solutions to the ADE in terms of strange eigenmodes. The composite spectral method is derived in Section 2 for a particular velocity field and Peclet number with homogeneous boundary conditions. Section 3 generalises the composite method to facilitate exploration of \mathcal{Q} , and numerical properties are reviewed (details are given in Appendix C). In Section 4, transport in the rotated arc mixer flow is solved, and in Section 5 these solutions are compared with solutions from a high resolution finite volume method. Section 6 gives conclusions and more general examples of composite flows.

2. Formal spectral solution of the advection–diffusion equation

To begin we expand ϕ and the ADE in the spectral space of the basis functions $\omega_n(\mathbf{x})$ of \mathcal{L}_1 over the spatial domain \mathcal{D} with appropriate boundary conditions, truncating the expansion at N terms. The approximate scalar field expansion is

$$\phi(\mathbf{x}, t) \approx \sum_{n=0}^{N-1} \Phi_n(t) \omega_n(\mathbf{x}), \quad (4)$$

which has the basis functions ordered such that the lowest energy modes are retained in (4). The ADE for the evolution of the spectral coefficients $\Phi_n(t)$ becomes an order N system of coupled ODEs

¹ If the α_0 mode is identically zero in the initial condition, the subscript becomes the minimum k for which $\alpha_k \neq 0$.

$$\frac{d\Phi}{dt} = \left(\mathbf{H}(t) - \frac{1}{Pe} \mathbf{D} \right) \Phi = \mathbf{A}(t) \Phi, \tag{5}$$

which is the spectral approximation of (1) for any velocity field. In (5), Φ is the vector of expansion coefficients, $\mathbf{H}(t)$ is an $N \times N$ matrix for the advection term $\mathbf{v} \cdot \nabla$, and \mathbf{D} is the constant diagonal $N \times N$ matrix of \mathcal{L}_1 eigenvalues μ_n^2 . The advection term transfers variance between wavenumbers, reflecting the potential for the flow to create small scale structure; countervailing diffusion irreversibly removes variance at a rate that increases with wavenumber. Because the flow is incompressible and does not penetrate the boundary ($\mathbf{v} \cdot \mathbf{n}|_{\partial D} = 0$), $H_{n,m}(t)$ is antisymmetric for general boundary conditions:

$$H_{n,m}(t) = - \int_D \omega_m(\mathbf{x}) \mathbf{v}(\mathbf{x}, t) \cdot \nabla \omega_n(\mathbf{x}) d^d \mathbf{x} = \int_D \omega_n(\mathbf{x}) \mathbf{v}(\mathbf{x}, t) \cdot \nabla \omega_m(\mathbf{x}) d^d \mathbf{x} = -H_{m,n}(t). \tag{6}$$

In (5), $\mathbf{A}(t)$ is the truncated spectral advection–diffusion operator; it has complex eigenvalues with negative real parts. As $Pe \rightarrow \infty$, $\mathbf{A}(t)$ becomes skew-symmetric with purely imaginary eigenvalues, corresponding to pure advection of the initial conditions. As $Pe \rightarrow 0$, $\mathbf{A}(t)$ becomes diagonal with purely real eigenvalues and no transfer between spectra.

The fundamental matrix solution $\mathbf{S}(t)$ of (5) satisfies

$$\Phi(t) = \mathbf{S}(t) \cdot \Phi(0), \tag{7}$$

with

$$\frac{d\mathbf{S}}{dt} = \mathbf{A}(t) \cdot \mathbf{S}(t). \tag{8}$$

Because the approximate velocity \mathbf{v} is piecewise constant in time, $\mathbf{A}(t)$ is also and so may be expressed as a composite of the steady operators \mathbf{A}_i

$$\mathbf{A}(t) = \begin{cases} \mathbf{A}_1 & 0 \leq t < t_1, \\ \mathbf{A}_2 & t_1 \leq t < t_2, \\ \vdots & \vdots \\ \mathbf{A}_n & t_{n-1} \leq t < t_n = T \end{cases} \tag{9}$$

$\mathbf{S}(T)$ is then given by the product of matrix exponentials:

$$\mathbf{S}(T) = \exp\{\mathbf{A}_1 t_1\} \cdot \exp\{\mathbf{A}_2(t_2 - t_1)\} \dots \exp\{\mathbf{A}_n(t_n - t_{n-1})\}, \tag{10}$$

and $\mathbf{S}(t)$ for $t < T$ is an appropriate truncation of these inner products. Aperiodic velocity fields can be handled by the method without alteration by considering $t \in [0, T]$ as the finite time over which solution of the ADE (1) is required. Continuous evaluation of (6)–(8) for a given $\mathbf{v}(\mathbf{x}, t; \chi)$ formally solves for the evolution of ϕ .

Floquet analysis of $\mathbf{S}(T)$ yields approximation of the NPPs φ_k . Denoting $\Gamma_k(t)$ as the vector of spectral expansion coefficients of φ_k in the same \mathcal{L}_1 basis, then from (2), these are related to $\Phi(t)$ by

$$\Phi(t) = \sum_{k=0}^K \alpha_k \Gamma_k(t) e^{\lambda_k t}. \tag{11}$$

Due to linearity, each individual product $\Gamma_k(t) e^{\lambda_k t}$ satisfies the ADE and thus Eq. (7). As the vectors $\Gamma_k(t)$ are also T -periodic, they are eigenvectors of the fundamental solution matrix $\mathbf{S}(t)$:

$$\Gamma_k(T) e^{\lambda_k T} = \mathbf{S}(T) \Gamma_k(0) = \Gamma_k(0) e^{\lambda_k T}. \tag{12}$$

As such, $\Gamma_k(0)$ and $\exp \lambda_k T$ are the normalized eigenvectors and -values of the matrix $\mathbf{S}(T)$ with the least negative eigenvalues corresponding to the slowest decaying NPPs. The NPP expansion coefficients for $t = [0, T]$ (and hence all t) can be calculated from $\Gamma_k(0)$ as

$$\Gamma_k(t) = e^{-\lambda_k t} \mathbf{S}(t) \Gamma_k(0). \tag{13}$$

After calculating \mathbf{S} , the coefficients for either ϕ or for as many of the φ_k as desired can be calculated and reconstructed in physical space. However, to continuously evaluate \mathbf{S} , or \mathbf{A} , is expensive because $\frac{1}{2}N^2$ integrals of (6) must be calculated and the matrix exponentials (10) must be estimated at each time step. More importantly, as we are interested in parametric variation, \mathbf{A} must be recalculated for a new $\hat{\mathbf{v}}$ at each new point in \mathcal{Q} . This is the fundamental difficulty in calculating global parametric solutions that we now turn to solve.

3. Composite spectral solution of the advection–diffusion equation over \mathcal{Q}

Instead of continuously recalculating $\mathbf{H}(t)$ and $\mathbf{S}(t)$ for each $\mathbf{v}(\mathbf{x}, t; \chi)$, it is far more efficient to exploit any symmetries of \mathbf{v} across χ . Of course, symmetries are not always present, but in many important cases they are. For example, many devices use periodic forcing (e.g. lid-driven cavity, journal bearing flow [23]) or reorientation (e.g. rotated arc mixer [21], ridged micromixers [30]) of a single fundamental velocity field to generate chaotic flow, though the full set of flow fields vary markedly over χ . Such is the case in many applications including chaotic advection and microfluidics where the flow regime is inherently Stokesian. Where symmetries or other relations reduce the full set of flows in \mathcal{Q} to effectively a smaller number, \mathbf{H} need be calculated *only once* for each fundamental flow. Then at each point in \mathcal{Q} , \mathbf{H} can be re-used to construct $\mathbf{S}(t)$ across \mathcal{Q} for the minimal cost of applying a symmetry operator, essentially a set of matrix operations. To belabor the point, where symmetry exists, so too do great computational efficiencies, and the composite spectral method makes full use of symmetries.

Prior to detailed description of the method, it is useful to illustrate how both symmetry operations and velocity field composition facilitate construction of a possibly large set of composite flows across χ from a very small set of fundamental underlying flows. We begin with velocity field composition, and denote N_χ as the total number of flows over χ under consideration. As such, the total number of points under consideration in \mathcal{Q} is $N_\mathcal{Q} = N_\chi N_{Pe}$, where N_{Pe} is the number of distinct Péclet numbers under consideration.

Approximation of the exact velocity field $\hat{\mathbf{v}}$ by the piecewise steady field \mathbf{v} involves composition of I steady component flows $\mathbf{v}_i(\mathbf{x})$:

$$\hat{\mathbf{v}}(\mathbf{x}, t; \chi) \approx \mathbf{v}(\mathbf{x}, t; \chi) \equiv \sum_i^I \mathbf{v}_i(\mathbf{x}) h_i(t; \chi_i). \quad (14)$$

The indicator function $h_i(t; \chi)$ equals one during the interval when $\mathbf{v}(\mathbf{x}, t; \chi) = \mathbf{v}_i(\mathbf{x})$ and zero otherwise (hence $\sum_i^I h_i(t; \chi) = 1$), and $h_i(t; \chi)$ is T -periodic, where T may vary with χ . $h_i(t; \chi)$ completely characterises each of the $N_\chi \geq I$ piecewise steady flows $\mathbf{v}(\mathbf{x}, t; \chi)$ by dictating how the I component flows \mathbf{v}_i are “welded” together. Increasing I makes (14) more accurate in general; however, for some classes of flow [29,24] (14) is exact.

In turn, the set of I steady component flows $\mathbf{v}_i(\mathbf{x})$ may be constructed from a subset of topologically fundamental flows via symmetry mappings. Call this set of $\bar{I} \leq I$ fundamental flows $\bar{\mathbf{v}}_i(\mathbf{x})$, then all the component flows $\mathbf{v}_i(\mathbf{x})$ are generated from $\bar{\mathbf{v}}_i(\mathbf{x})$ via the general mapping operator \mathcal{M}_i :

$$\mathbf{v}_i(\mathbf{x}) = \mathcal{M}_i[\bar{\mathbf{v}}_1(\mathbf{x}), \dots, \bar{\mathbf{v}}_{\bar{I}}(\mathbf{x})], \quad i = 1 : I. \quad (15)$$

What symmetries can be incorporated into the composite spectral calculation? We will use the mapping operations of reorientation, reflection, scaling, and superposition. Due to their different characteristics, reflection/reorientation are put into the algorithm differently from scaling/superposition. No general algorithm exists to determine the best set of fundamental flows and symmetries with which to compose the full set of flows within \mathcal{Q} , and this gives flow designers great freedom to invent simply driven flows and their symmetric extensions to accomplish various purposes.

Defining \mathcal{R}_i and \mathcal{S}_i respectively as reorientation/reflection and scaling/superposition, \mathcal{M}_i may be decomposed without loss of generality as

$$\mathcal{M}_i = \mathcal{M}_{i_0} \circ \mathcal{M}_{i_1} \circ \dots \circ \mathcal{M}_{i_n}, \quad = \mathcal{R}_{i_0} \circ \mathcal{S}_{i_0} \circ \mathcal{R}_{i_1} \circ \mathcal{S}_{i_1} \circ \dots \circ \mathcal{R}_{i_n} \circ \mathcal{S}_{i_n}, \quad (16)$$

where the operators $\mathcal{R}_i, \mathcal{S}_j$ do not commute. Of course, a particular problem may have one type of symmetry or the other, or it may have both or none. For brevity, we will discuss simpler mappings of the form

$$\mathcal{M}_i = \mathcal{R}_i \circ \mathcal{S}_j, \quad (17)$$

which, nevertheless, encompasses a wide class of problems by itself; the method below holds for the general case. As \mathcal{R}_i and \mathcal{S}_j do not commute, multiple \mathcal{S}_j and \mathcal{R}_i mappings must be ordered correctly. Applying \mathcal{S}_j first creates an intermediate set of \tilde{T} velocities $\tilde{\mathbf{v}}_i(\mathbf{x})$, then application of \mathcal{R}_i creates the component flows $\mathbf{v}_i(\mathbf{x})$:

$$\{\bar{\mathbf{v}}_i(\mathbf{x})\} \xrightarrow{\mathcal{S}_j} \{\tilde{\mathbf{v}}_i(\mathbf{x})\} \xrightarrow{\mathcal{R}_i} \{\mathbf{v}_i(\mathbf{x})\}. \tag{18}$$

Appendix B shows an example of using \mathcal{S}_i and \mathcal{R}_i to compose the general flows of a lid-driven cavity.

As these mappings define the way in which the set of I component flows are constructed from the set of the set of \tilde{T} fundamental flows, any component flow in \mathcal{Q} may be constructed from the $\bar{\mathbf{v}}_i$ as

$$\mathbf{v}_i(\mathbf{x}) = \mathcal{R}_i[\mathcal{S}_j[\bar{\mathbf{v}}_1(\mathbf{x}), \dots, \bar{\mathbf{v}}_{\tilde{T}}(\mathbf{x})]], \tag{19}$$

and subsequently any piecewise steady velocity field \mathbf{v} in \mathcal{Q} can be constructed from the \mathbf{v}_i via (14).

The sequence of mappings and compositions building $\mathbf{v}(\mathbf{x}, t; \chi)$ from $\{\bar{\mathbf{v}}_i(\mathbf{x})\}$ is illustrated in Fig. 1, where application of the mappings (19) and composition via (14) result in increasingly larger sets of flows. Note that composition (14) and superposition operations are many-to-many, while scaling and rotation/reflection are one-to-many. Although in principle it is possible to construct an infinite set of flows $\mathbf{v}(\mathbf{x}, t; \chi)$ via these operations, in practice a finite number (specifically N_χ) are required due to both the desired level of resolution \mathcal{Q} and characteristics of the application at hand.

Efficiency of the composite spectral method arises from performing computations at the highest possible levels in Fig. 1, such that individual steps scale with I , \tilde{T} , \bar{T} , or N_χ and the inequality $\bar{T} \leq \tilde{T} \leq I \leq N_\chi$ optimises the numerics. The recipe for the composite spectral method is outlined as follows, the details of whose steps are described below.

- Step 1.** Approximate the exact velocity field $\hat{\mathbf{v}}(\mathbf{x}, t; \chi)$ via the piecewise steady velocity field $\mathbf{v}(\mathbf{x}, t; \chi)$, comprised of the steady component flows $\mathbf{v}_i(\mathbf{x})$ (Eq. (14)).
- Step 2.** Identify the (small set of) fundamental flows $\bar{\mathbf{v}}_i(\mathbf{x})$ from which all component flows can be derived through symmetry (Eq. (18)).
- Step 3.** Calculate the advection operators $\bar{\mathbf{H}}_i$ for the \bar{T} fundamental flows (Eq. (6)).
- Step 4.** Calculate the matrix exponential $\exp(\bar{\mathbf{H}}_i)$ for the \bar{T} fundamental flows (Eq. (23)).
- Step 5.** Calculate the matrix solution $\tilde{\mathbf{S}}_{j,Pe}(t)$ for the \tilde{T} intermediate flows (Eq. (23)).
- Step 6.** Calculate the matrix solution $\mathbf{S}_{i,Pe}(t)$ for the I component flows (Eq. (23)).
for each point in \mathcal{Q}
- Step 7.** Compose the composite flow fundamental matrix solution $\mathbf{S}(t; \chi, Pe)$ from the solutions $\mathbf{S}_{i,Pe}(t)$ (Eq. (25)).

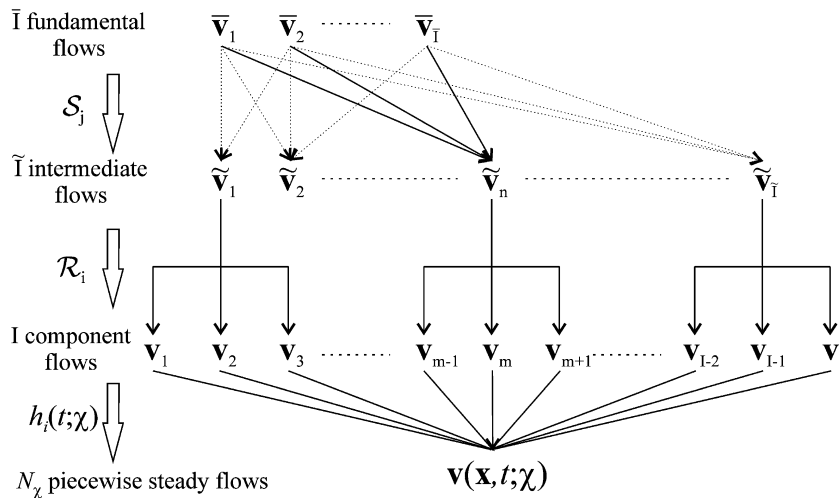


Fig. 1. Construction of piecewise steady flows $\mathbf{v}(\mathbf{x}, t; \chi)$ from fundamental steady flows $\bar{\mathbf{v}}_i(\mathbf{x})$ by scaling/superposition \mathcal{S}_j , rotation/reflection \mathcal{R}_i and composition via $h_i(t; \chi)$ in (14).

Step 8. Calculate M leading eigenvalues and eigenvectors, which correspond to the principal NPPs, of $\mathbf{S}(t; \chi, Pe)$ (Eq. (12)).
end

Step 1 is composition of $\mathbf{v}(\mathbf{x}, t; \chi)$ via Eq. (14).

Step 2 is deciding on a set of fundamental flows $\tilde{\mathbf{v}}_i(\mathbf{x})$ and associated mapping operators $\mathcal{S}_j, \mathcal{R}_i$ to construct the full set of component flows $\mathbf{v}_i(\mathbf{x})$, as per (18).

Step 3 is to compute the operators $\bar{\mathbf{H}}_i$ with Eq. (6) for each of the \bar{I} fundamental flows $\tilde{\mathbf{v}}_i(\mathbf{x})$. From these fundamental flow operators, the intermediate and component operators $\tilde{\mathbf{H}}_i, \mathbf{H}_i$ can subsequently be constructed via the scaling/superposition and rotation/reflection mappings respectively:

$$\tilde{\mathbf{H}}_j = \mathcal{S}_j[\bar{\mathbf{H}}_1, \dots, \bar{\mathbf{H}}_7] = \sum_i s_{i,j} \bar{\mathbf{H}}_i, \quad (20)$$

$$\mathbf{H}_i = \mathcal{R}_i[\tilde{\mathbf{H}}_j] = \mathbf{R}_i \cdot \tilde{\mathbf{H}}_j \cdot \mathbf{R}_i^{-1}, \quad (21)$$

where $s_{i,j}$ are scaling factors inherent to the piecewise steady approximation (14), and \mathbf{R}_i is the orthogonal rotation/reflection matrix corresponding to \mathcal{R}_i . As such, the component flow matrix solution $\mathbf{S}_{i,Pe}(t)$ is explicitly

$$\mathbf{S}_{i,Pe}(t) = \exp \left\{ \left(\mathbf{H}_i - \frac{1}{Pe} \mathbf{D} \right) t \right\} = \exp \left\{ \left(\mathcal{R}_i[\mathcal{S}_j[\bar{\mathbf{H}}_1, \dots, \bar{\mathbf{H}}_7]] - \frac{1}{Pe} \mathbf{D} \right) t \right\}, \quad (22)$$

which must be calculated for different values of $\{s_{i,j}\}$, Pe , and for various $t \in [0, T]$ (specific values of t are governed by (14)). Explicit computation of this exponential is expensive, but significant efficiencies arise if the mapping operators can be applied *a posteriori*, then exponentiation need only be performed once for each fundamental flow. Conceptually, we require the augmented rotation and scaling operators \mathcal{R}_i^* and \mathcal{S}_j^* , such that (22) can be written

$$\mathbf{S}_{i,Pe}(t) = \mathcal{R}_i^*[\mathcal{S}_j^*[\exp(\bar{\mathbf{H}}_1 t), \dots, \exp(\bar{\mathbf{H}}_7 t), \exp(\mathbf{D} t)]] = \mathcal{R}_i^*[\tilde{\mathbf{S}}_{j,Pe}(t)]. \quad (23)$$

Step 4 : Assuming $\mathcal{R}_i^*, \mathcal{S}_j^*$ exist and can be determined, the exponentials $\exp(\bar{\mathbf{H}}_i t)$ need to be calculated ($\exp(\mathbf{D} t)$ is trivial). Although matrix exponentiation is expensive, as the operator \mathcal{S}_j^* only requires calculation of $\exp(\bar{\mathbf{H}}_i \delta t)$ for the short time δt , a Taylor series method (see Appendix D) is available.

Step 5 involves application of the augmented scaling/superposition operator \mathcal{S}_j^* . The short time matrix solution $\tilde{\mathbf{S}}_{j,Pe}(\delta t)$ for the intermediate flows $\tilde{\mathbf{v}}_j(\mathbf{x})$ is calculated from the exponentials in Step 4, and subsequently these results are scaled up to $\tilde{\mathbf{S}}_{j,Pe}(t)$ for the required values of $t \in [0, T]$. The methods of Suzuki [31] and Zhong [34] facilitate this with minimal computation; details are given in Appendix C, so defining \mathcal{S}_j^* .

Step 6 involves application of the augmented rotation/reflection operator \mathcal{R}_i^* . As diffusion is isotropic (the operator \mathbf{D} is diagonal), \mathcal{R}_i in (22) may be expanded to include $\frac{1}{Pe} \mathbf{D}$ without change. As per (21), the rotation/reflection operator involves a similarity transform. Since the exponential of a similarity transform is equal to the similarity transform of the exponential, $\mathcal{R}_i^* = \mathcal{R}_i$, and so rotation/reflection can be simply applied by matrix multiplication post exponentiation:

$$\mathbf{S}_{i,Pe}(t) = \mathbf{R}_i \cdot \tilde{\mathbf{S}}_{j,Pe}(t) \cdot \mathbf{R}_i^{-1}. \quad (24)$$

Step 7 follows composition of the solution matrix \mathbf{S} in (9); here the fundamental matrix $\mathbf{S}(T; \chi, Pe)$ for $\mathbf{v}(\mathbf{x}, t; \chi)$ and Pe is given by the inner product

$$\mathbf{S}(T; \chi, Pe) = \mathbf{S}_{i_1, Pe}(t_1) \cdot \mathbf{S}_{i_2, Pe}(t_2 - t_1) \dots \mathbf{S}_{i_{N_T}, Pe}(t_{N_T} - t_{N_T-1}), \quad (25)$$

where for each element in χ , the set $\{(i_1, t_1), \dots, (i_{N_T}, t_{N_T})\}$ completely characterises the indicator function $h_f(t; \chi)$ in (14), i.e. $\mathbf{v}(\mathbf{x}, t; \chi) = \mathbf{v}_{i_j}(\mathbf{x})$ if $t_{j-1} \leq t < t_j$. For $t < T$ the fundamental matrix $\mathbf{S}(t; \chi, Pe)$ is given by appropriate truncation of these inner products.

Step 8 follows Eq. (12): approximations of the M dominant NPPs are given by the leading M eigenvalues and eigenvectors of $\mathbf{S}(T; \chi, Pe)$, which can be reconstructed in physical space to obtain φ_k .

Details of the accuracy and computational expense of the composite spectral method are given in [Appendix C](#) for the general case involving all possible combinations for mappings of the form (17). As these mappings admit a wide class of problems, optimal protocols for storage and computation cannot be prescribed, and in many applications further computational savings arise due to omission or reduction of particular steps. The method is very efficient if the number of fundamental flows \bar{I} is low and the number of intermediate flows \tilde{I} moderate. In such cases, Step 8 involves the bulk of computation, which scales with $N_{\mathcal{Q}}$. Solution of this eigenproblem is expensive for large N , and ultimately places practical upper bounds on the Peclet number, however other numerical methods share similar restrictions. All of the method steps are inherently parallelisable to a high degree.

4. Composite spectral method case study: global parametric transport solutions for a chaotic flow

To illustrate both the richness of the ADE global solutions space and implementation of the composite spectral method, we will use the 2D time-periodic Rotated Arc Mixer (RAM) flow [21]. Illustrated in [Fig. 2](#), the RAM confines fluid within a circular domain of radius R that has one boundary arc on which there is a constant tangential boundary velocity $R\Omega$; the boundary velocity is zero outside of this aperture of angular opening Δ . In the fluid domain the boundary motion drives a cavity flow; for a Newtonian fluid in Stokes flow Hwu et al. [11] derived an analytic expression for the streamfunction. As chaos in 2D flows requires some time-dependence, for the RAM at integer multiples of time τ/Ω the aperture instantaneously rotates through an angle Θ to a new position ([Fig. 2](#)), periodically reorienting the flow. We non-dimensionalize the problem by introduction of the dimensionless variables $r' = r/R$, $t' = t\Omega$, $\mathbf{v}' = \mathbf{v}/R\Omega$, $Pe = R^2\Omega/D$ and immediately drop the primes, henceforth referring to dimensionless variables only. In the Stokes limit Ω drops out of the dimensionless formulation, and the flow reorients every dimensionless time τ . If $\Theta/2\pi = p/q$ for integers p , q , then $T = q\tau$ and q aperture reorientations occur within each period, and the flow is T -periodic for rational values of p/q .

The RAM is one of a variety of laminar flow devices [30] that generate chaotic flows. Studies of these devices have not extensively explored their transport properties as a function of the controlling parameters. To our knowledge, this is the first detailed parametric study of a physically realisable flow. A Newtonian, incompressible fluid undergoing Stokes flow is considered here,² in which case the dimensionless advective velocity field is completely characterised by the set $\chi = \{\tau, \Theta, \Delta\}$, forming the four-dimensional parameter space \mathcal{Q} along with the Peclet number Pe . The dimensions of the parameter space are $\mathcal{Q} : \{\tau, \Delta, \Theta, Pe\} = (0, \infty) \times [0, 2\pi] \times [-\pi, \pi] \times [0, \infty)$. If N_{τ} , N_{Θ} , N_{Δ} , N_{Pe} respectively are the resolutions of τ , Θ , Δ , Pe in \mathcal{Q} , then the number of points in \mathcal{Q} is $N_{\mathcal{Q}} = N_{\tau}N_{\Theta}N_{\Delta}N_{Pe}$. As the velocity of the RAM consists of temporal reorientations of the initial flow field, flows within the device are only topologically distinct for distinct values of the aperture opening Δ . As such, the number of base flows of the 2D RAM over \mathcal{Q} is $\bar{I} = N_{\Delta}$. Mapping of the base flows $\bar{\mathbf{v}}(\mathbf{x})$ in the 2D RAM consists solely of rotation, so in this case the mapping operator simplifies to $\mathcal{M}_i = \mathcal{R}_i$, and the advective velocity (in this case exact) is

$$\mathbf{v}(\mathbf{x}, t; \chi) = \sum_i^I \mathcal{R}_i[\bar{\mathbf{v}}_i(\mathbf{x})]h_i(t; \chi), \quad (26)$$

where I is the total number of steady distinct flows in the RAM over the set \mathcal{Q} . The advection–diffusion operator $\mathbf{S}(T; \chi, Pe)$ over a full period T of the RAM is composed of q reoriented operators;

$$\mathbf{S}(T; \chi, Pe) = \mathbf{S}_{q-1} \cdot \mathbf{S}_{q-2} \dots \mathbf{S}_0, \quad (27)$$

$$\mathbf{S}_n = \mathbf{R}_{\Theta}^n \cdot \mathbf{S}_0 \cdot \mathbf{R}_{\Theta}^{-n}, \quad (28)$$

² Cases where inertial or Non-Newtonian effects are significant, or where the flow field is determined numerically or experimentally can all be handled by the method; the sole requirement is that the scalar is passive. If the viscous timescale R^2/μ is small with respect to the reorientation frequency $1/\tau\Omega$, then transient effects of the velocity field associated with aperture reorientations as quantified by the Strouhal number $St = Re/\tau$ may be ignored. If the Reynolds number $Re = \Omega R^2/\mu$ is negligible, the advective velocity field $\mathbf{v}(\mathbf{x}, t; \chi)$ is temporally piecewise constant for say $\tau > 10^{-3}$.

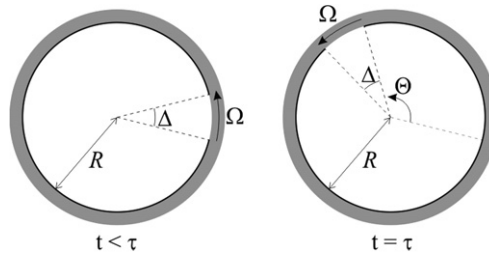


Fig. 2. Rotated arc mixer (RAM) flow geometry and parameters.

where \mathbf{S}_{n-1} is the advection–diffusion operator for the n th cell and \mathbf{R}_Θ is the rotation operator corresponding to offset angle Θ . Following Speetjens et al. [29], as $\mathbf{R}_\Theta^q = \mathbf{I}$, the fundamental matrix $\mathbf{S}(T; \chi, Pe)$ simplifies to

$$\mathbf{S}(T; \chi, Pe) = (\mathbf{R}_\Theta^{-1} \cdot \mathbf{S}_0)^q = \left(\mathbf{R}_\Theta^{-1} \cdot \exp \left\{ \tau \left(\bar{\mathbf{H}}_\Delta + \frac{1}{Pe} \mathbf{D} \right) \right\} \right)^q, \quad (29)$$

where $\bar{\mathbf{H}}_\Delta$ is the advective operator corresponding to \bar{v}_i for an aperture opening of Δ . As such, eigen-analysis of the advection–diffusion operator may be performed over one cell only

$$\mathbf{S}^*(\tau; \chi, Pe) = \mathbf{R}_\Theta^{-1} \cdot \exp \left\{ \tau \left(\bar{\mathbf{H}}_\Delta + \frac{1}{Pe} \mathbf{D} \right) \right\}, \quad (30)$$

where \mathbf{S}^* is in a rotating frame moving with the window opening, and so eigenvectors of \mathbf{S}^* require subsequent rotation by \mathbf{R}_Θ to return to the laboratory frame. Simplification of (29) to (30) eliminates the need to calculate the full fundamental matrix $\mathbf{S}(T; \chi, Pe)$, which is cumbersome for large q , and furthermore facilitates computation for irrational values of Θ/π .

Application of the method over the points in \mathcal{Q} involves calculation of the advective operator (Step 3 of the method) N_Δ times. The exponential in (30) is determined for short time $\tau = \delta t$ and different values of Δ and Pe (Step 4), using (D.2) N_Δ times and (D.3) $N_\Delta \times N_{Pe}$ times. The results are then scaled (Step 5d) to any τ using (D.5), and the substeps 5a–5c in Table C.1 omitted. The reorientation mapping (Step 6) must be performed $N_\Delta \times N_\Theta \times N_{Pe}$ times, and Step 7 is omitted by utilisation of the symmetry solution above. Only Step 8 need be solved for each unique point in \mathcal{Q} , so the eigenproblem is solved $N_\mathcal{Q}$ times. The composite spectral method is particularly efficient for this application as the temporally piecewise constant velocity approximation is exact, the mapping operator involves reorientation only, plus further simplification from symmetry of the q reorientations. As the matrix exponential and eigenproblem steps can be solved to high accuracy, and the exact velocity field \hat{v} is piecewise steady, the major source of error in this application arises from truncation of the spectral expansion (4) to N terms. Though the RAM is a particularly simple flow, many other applications would enjoy similar efficiencies.

The dominant strange eigenmodes of the ADE (1) with homogeneous Dirichlet boundary conditions ($\phi = 0$) are calculated over a large subset of the entire space \mathcal{Q} for the RAM. For simplicity we fix the window opening to $\Delta = \pi/4$, so there is only one fundamental flow: $\bar{v} = 1$. The eigenfunctions of \mathcal{L}_1 over the unit circle are the Fourier–Bessel functions

$$\omega_n(r, \theta) = \sqrt{\frac{2}{\pi}} \frac{J_p(\alpha_{p,q} r)}{J_{p+1}(\alpha_{p,q})} \cdot \begin{cases} \frac{1}{\sqrt{2}} & p = 0, \\ \cos p\theta & n \text{ even}, \\ \sin p\theta & n \text{ odd}, \end{cases} \quad (31)$$

where J_p is the p th order Bessel function of the first kind, and $\alpha_{p,q}$ is the q th zero of J_p . If the integers $p \in [0:N_m]$, and $q \in [1:N_m]$, where $1/N_m$ is the spectral resolution, the number of spectral modes is $N = 2N_m^2 + N_m$. The RAM dimensionless velocity field boundary condition is

$$\mathbf{v}(r, \theta, t)|_{r=1} = \left\{ 0, H\left(\theta - \Theta \left\lfloor \frac{t}{\tau} \right\rfloor - \frac{\Delta}{2}\right) - H\left(\theta - \Theta \left\lfloor \frac{t}{\tau} \right\rfloor + \frac{\Delta}{2}\right) \right\}, \quad (32)$$

where H is the Heavyside function, and $\lfloor x \rfloor$ denotes the integer part of x . As the advective velocity field is temporally piecewise constant, the steady two-dimensional solution of Hwu et al. [11] for this boundary condition in terms of the stream function $\psi(r, \theta, t); \mathbf{v} = \nabla \times \psi \mathbf{e}_z$ can be generalised to the temporal field

$$\begin{aligned} \psi(r, \theta, t) &= \frac{1-r^2}{2\pi} \left\{ g\left(\Theta \left\lfloor \frac{t}{\tau} \right\rfloor + \frac{\Delta}{2}\right) - g\left(\Theta \left\lfloor \frac{t}{\tau} \right\rfloor - \frac{\Delta}{2}\right) \right\}, \quad \text{where } g(\alpha) \\ &= \arctan \left[\frac{(1+r^2+2r\cos\theta)\tan\frac{\alpha}{2} - 2r\sin\theta}{1-r^2} \right]. \end{aligned} \tag{33}$$

The advection coefficients (6) can be simplified with the streamfunction to

$$\hat{H}_{n,m} = - \int_{\mathcal{D}} \omega_m(\mathbf{x}) \hat{\mathbf{v}}(\mathbf{x}, 0) \cdot \nabla \omega_n(\mathbf{x}) d^2 \mathbf{x} = - \int_{\mathcal{D}} \psi(\mathbf{x}, 0) \hat{\mathbf{e}}_z \cdot \{ \nabla \omega_n(\mathbf{x}) \times \nabla \omega_m(\mathbf{x}) \} d^2 \mathbf{x} = - \hat{H}_{m,n}. \tag{34}$$

For these stream- and eigenfunctions, the θ -component of the integral has an analytic solution; however, the r -component must be computed numerically for each distinct pair $\{\omega_n, \omega_m\}$. The r -integral in (34) is solved numerically using the collocation method of Levin [18] described in Appendix C, where the recurrent Bessel function products $J_p J_r, J_{p-1} J_r, J_p J_{r-1}, J_{p-1} J_{r-1}$ arising from the gradient cross-product plays the role of $Q_n(x)$ and ψ has the role of $P(x)$ in (C.4).

Calculating the matrix exponential (30) for various values of Pe and t using (D.2) and (D.5) with subsequent multiplication by the rotational operator \mathbf{R}_Θ calculates the order N fundamental matrix $\mathbf{S}(\tau; \chi, Pe)$ for any point in \mathcal{Q} . Estimation of the dominant strange eigenmode ($M = 1$) of ϕ corresponds to calculation of the leading eigenvalue $\exp \lambda_0 \tau$ and eigenvector $\Gamma_0(0)$ of $\mathbf{S}(\tau; \chi, Pe)$. To determine λ_0, φ_0 over the space $\tau \times \Theta \times Pe$ to resolution $N_\tau \times N_\Theta \times N_{Pe}$, calculation of N_Θ rotational matrices \mathbf{R}_Θ and $N_{Pe} N_\tau$ fundamental matrices $\mathbf{S}_{0,Pe}(t)$ is required, followed by solution of $N_\tau N_\Theta N_{Pe}$ order N eigenproblems.

We define the transport enhancement factor $-\lambda_0 Pe / \alpha_{0,1}^2$ as the ratio of decay rates of the dominant eigenmodes for the \mathcal{L}_2 and \mathcal{L}_1 operators in the disc, the latter of which is $\alpha_{0,1}^2 / Pe$, the asymptotic transport rate for diffusion. In practical terms, the transport enhancement factor gives the ratio of transport acceleration over diffusion only in the asymptotic (long-time limit). Fig. 3 is a contour plot of the transport enhancement factor over the parameter space $\tau \times \Theta$ at $Pe = 10^3$, calculated at a resolution $N_\tau \times N_\Theta = 120 \times 1000$ with a spectral resolution $N_m = 20$ ($N = 820$ spectral modes).

Transport enhancement ranges from 1 (no enhancement) to slightly more than 6-fold improvement; note the vertical axis and contour graduation are logarithmic. Distribution of the enhancement factor over \mathcal{Q} in Fig. 3 is fractal, and contains many localised maxima. Behaviour over this parameter space is rich; spatial symmetry locking similar to frequency-locking in Arnol'd tongues [6] occurs in the tongues emanating from

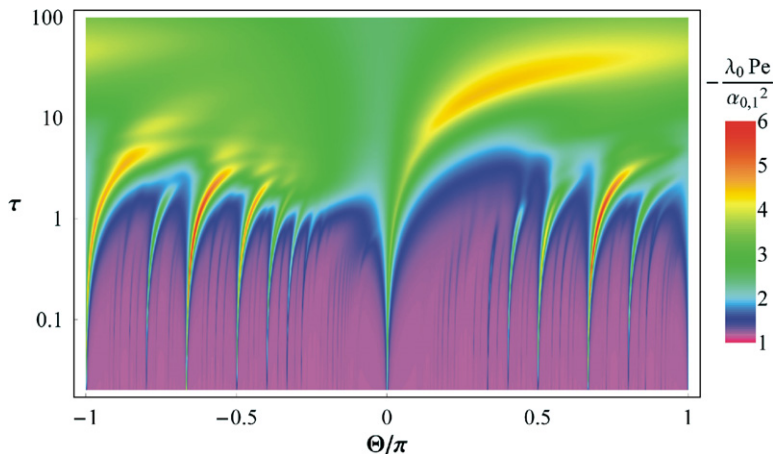


Fig. 3. Map of the transport enhancement factor $-\lambda_0 Pe / \alpha_{0,1}^2$ for the RAM flow and Dirichlet boundary conditions over the parameter range $\tau \in [0.01, 100]$, $\Theta \in [-\pi, \pi]$, $\Delta = \frac{\pi}{4}$, $Pe = 10^3$. Note logarithmic scaling of the τ axis and $-\lambda_0 Pe / \alpha_{0,1}^2$ contours.

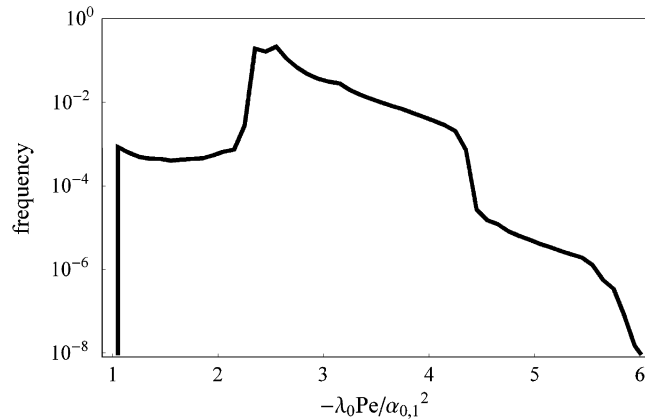


Fig. 4. Probability density function of the transport enhancement factor $-\lambda_0 Pe/\alpha_{0,1}^2$ for the RAM flow and Dirichlet boundary conditions over the parameter range $\tau \in [0.01, 500]$, $\Theta \in [-\pi, \pi]$, $\Delta = \frac{\pi}{4}$, $Pe = 10^3$. Note logarithmic scaling of the vertical axis.

Table 1
Test mixing cases

Mix case	Θ	τ	Δ	Chaotic mixing characteristics
Case 1	$-\frac{3\pi}{5}$	8	$\frac{\pi}{4}$	Globally well mixed
Case 2	$\frac{2\pi}{5}$	7	$\frac{\pi}{4}$	Domain mostly non-mixing
Case 3	$\frac{3\pi}{5}$	4	$\frac{\pi}{4}$	Single large island
Case 4	$-\frac{3\pi}{5}$	5	$\frac{\pi}{4}$	Small island chain

rational values of Θ/π at $\tau = 0$, and an order–disorder transition occurs along the tongues at $\tau \sim 1$. The global optimum occurs in a tongue, corresponding to a highly ordered symmetric eigenmode. Due to the existence of multiple local optima of λ_0 and the fractal structure at low τ , many fast optimization techniques would fail to locate the global optimum within \mathcal{Q} . To elucidate the global structure of transport over the control parameter space and confidently identify this global optimum, high resolution global exploration of \mathcal{Q} is necessary. Localisation of optima is highlighted further by the probability distribution function of the transport enhancement factor over the range $\tau \in [0.01, 500]$, $\Theta \in [-\pi, \pi]$ in Fig. 4; regions where $-\lambda_0 Pe/\alpha_{0,1}^2 > 4$ covers than 10^{-3} of \mathcal{Q} .

Calculation of φ_0 and λ_0 over the 1.2×10^5 points in Fig. 3 using the composite spectral method took about 1.05×10^6 s of computation on an Intel[®] Xeon[™] 3.00 GHz CPU using Matlab 7.0.4. Calculation of the $H_{n,m}$ is about 8% of the total computation time, solution of the fundamental matrices using Zhong’s [34] method less than 1%, and the remainder was used to solve the eigenproblem for each point in \mathcal{Q} . For comparison, a single value of λ_0 for $Pe = 10^3$ determined to similar accuracy by observation of the long time solution using a finite volume method (with the velocity field specified analytically) implemented under the CFD software CFX 5.7.1[™] required 5.1×10^4 s of computation on the same processor. In this case the composite spectral method is approximately 6000 times more efficient in determining global parametric transport solutions. Similar efficiencies are possible for many systems with a set of naturally composable flows.

5. Pattern convergence

To quantify accuracy and investigate convergence properties of the composite spectral method, we consider solutions for the RAM flow for the four sets of parameters $\chi = \{\Delta, \tau, \Theta\}$ in Table 1, which represent different “mixing cases” for the device. These cases have qualitatively different mixing characteristics in the case of pure advection, as reflected in the Poincaré sections in Fig. 5a–d.

To study the influence of Pe on solution accuracy the Peclét number range $Pe = 10^2, 10^3, 10^4$ is considered for a set of spectral resolutions $N_m = 20, 30, 40, 50$. The dominant NPP φ_0 at integer multiples of τ for each of the mixing cases at $Pe = 10^4$ as calculated by the composite spectral method for $N_m = 50$, is depicted in

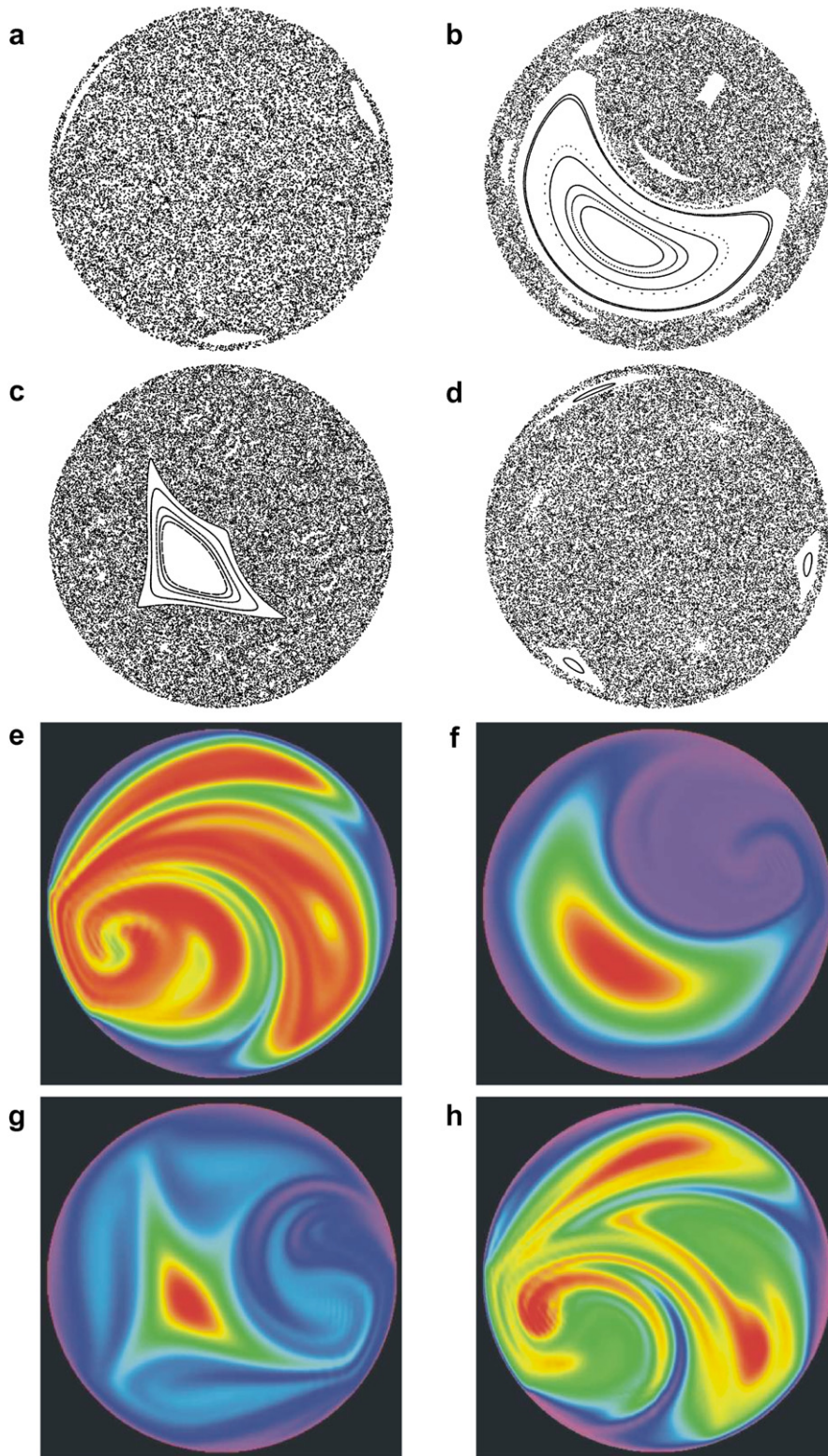


Fig. 5. (a) case 1, (b) case 2, (c) case 3, (d) case 4, (e) case 1, (f) case 2, (g) case 3 and (h) case 4. Poincaré sections (a–d) and dominant strange eigenmodes at $Pe = 10^4$ (e–h) for mixing cases 1–4.

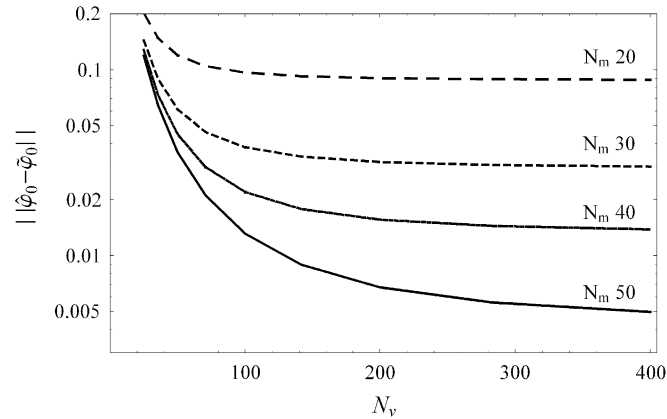


Fig. 6. L_2 norm of error between spectral method dominant strange eigenmode $\tilde{\phi}_0(\mathbf{x}, t)$ calculated in CFXTM 5.7.1. for different finite volume mesh resolutions N_v , and reference solutions $\hat{\phi}_0(\mathbf{x}, t)$ for $N_m = 20, 30, 40, 50$ for mix case 3 at $Pe = 10^4$.

Fig. 5e–h, where blue $\phi = 0$ at the domain boundary. Some evidence of aliasing (or Gibbs phenomena) exists in cases 1 and 4, suggesting insufficient spectral modes to resolve the full solution structure in these cases. These results illustrate the diversity of structure in the ADE dynamics across the parameter space. In some cases structures (KAM tori, chaotic sea) in the pure advection cases (Poincaré sections) apparently carry over to the scalar distribution, while in other cases structure in the scalar distribution has no obvious correspondent to the Poincaré section. Large-scale structure in the flow advection pattern is reflected in the scalar transport pattern, but small scale structure is not. Also of note are the large internal gradients of ϕ within \mathcal{D} , especially those near the boundaries in cases 1 and 4. As diffusion acts to smooth these gradients created by advection, structural complexity increases with Pe , and scaling arguments suggest striation thickness scales as $1/\sqrt{Pe}$. In the limit $Pe \rightarrow \infty$, striation thickness becomes infinitesimal, as happens for pure advection in chaotic regions.

Prior to investigation of the convergence properties of the composite spectral method, it is necessary to verify that the composite spectral method results converge to the correct solution. Not having analytic solutions to the ADE for the RAM, we utilise CFD solutions from the commercial package CFXTM 5.7.1 that have converged in terms of mesh resolution. We define the finite volume mesh resolution N_v in CFX as the domain radius divided by the maximum mesh element length, and the dominant NPP for case 3 at $Pe = 10^4$ (denoted $\tilde{\phi}_0$) is calculated in CFX over the range $N_v = 25 - 400$ using time steps small enough to eliminate transient errors. These results are compared with the same NPP $\hat{\phi}_0$ calculated using the composite spectral method over the range $N_m = 20 - 50$. The L_2 norm of the error between these results over the domain \mathcal{D} and time interval $t \in [0, \tau]$ is shown in Fig. 6. This error converges steadily with increasing N_m and N_v , and from the results of Fig. 6 it is expected that this error approaches zero as $N_m, N_v \rightarrow \infty$. This is taken as verification that the composite spectral method converges to the correct solution. The main source of error in the finite volume solution arises from spurious numerical diffusion, whereas aliasing generates the bulk of errors in the composite spectral method. Both of these errors decrease with increasing resolution, however a greater resolution is required in the finite volume method to achieve the same solution precision.

Using the spectral mesh resolution $N_m = 50$ as a reference solution, the spectral convergence properties of the composite spectral method may be examined. The L_2 norm over the spatial domain \mathcal{D} and time period τ of the dominant NPP error for the lower resolution ($N_m = 20 - 40$) solutions are shown in Figs. 7–9 for each mixing case and Peclét number. In all cases the L_2 error decays faster than algebraically with N_m^{-1} , and near-linear trends are observed in the log-linear plots. As expected, the composite spectral method exhibits close to spectral accuracy: the errors decay exponentially with spectral resolution N_m . Of particular note is the difference in accuracy across mixing cases; as seen in Fig. 5, structural complexity may vary significantly with control parameters for fixed Peclét number. The error spread increases with Pe and in some cases the difference is an order of magnitude. As such the minimum spectral resolution N_m must be determined with respect to minimum striation thickness across all strange eigenmodes over \mathcal{Q} at fixed Pe . Figs. 7–9 suggest that for minimum error in $\hat{\phi}_0$, a spectral mesh resolution $N_m \approx 30 - 40$ is suitable for $Pe = 10^2 - 10^3$, but not

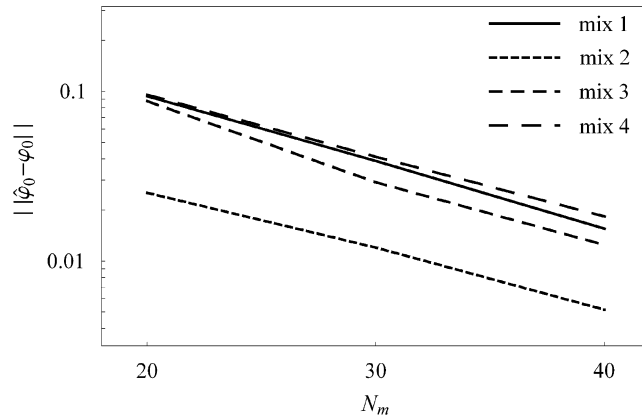


Fig. 7. L_2 norm of error between spectral method dominant strange eigenmode $\hat{\varphi}_0(\mathbf{x}, t)$ and reference $N_m = 50$ solution φ_0 for $Pe = 10^4$.

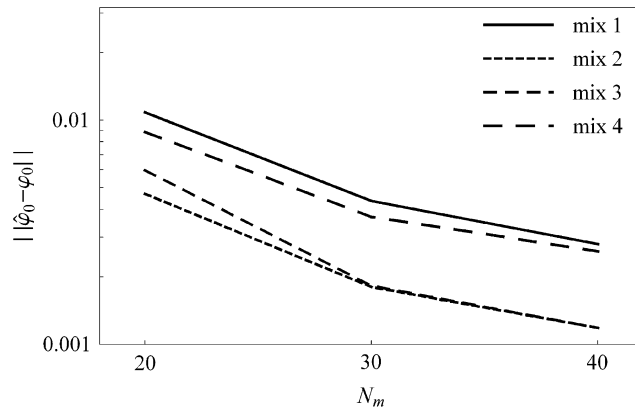


Fig. 8. L_2 norm of error between spectral method dominant strange eigenmode $\hat{\varphi}_0(\mathbf{x}, t)$ and reference $N_m = 50$ solution φ_0 for $Pe = 10^3$.

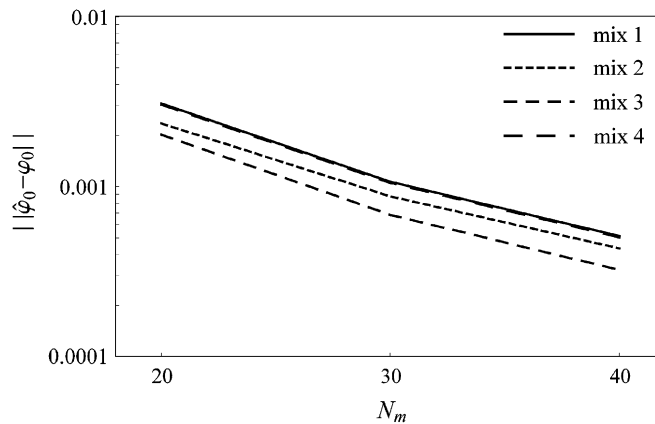


Fig. 9. L_2 norm of error between spectral method dominant strange eigenmode $\hat{\varphi}_0(\mathbf{x}, t)$ and reference $N_m = 50$ solution φ_0 for $Pe = 10^2$.

sufficient for higher Péclet numbers. The low resolution (N_m) used here is not expected to resolve solutions for substantial Péclet numbers, but rather to establish the convergence properties of the method. The relationship between N_m and Pe is investigated in detail by Adrover et al. [1], where spectral accuracy is observed and for fixed accuracy, N_m scales as Pe^β , where β is dependant upon the mixing protocol at hand.

As the dominant strange eigenmode decay rate λ_0 is a function of spatial and temporal averages of the dominant strange eigenmode φ_0 , its gradient and L_2 norms [19], it is anticipated that λ_0 may be predicted to greater accuracy than φ_0 due to the averaging process. This behaviour is evident in the convergence analysis, where errors between the λ_0 for the reference solution and $N_m = 20, 30, 40$ for all mixing cases and Peclet numbers is shown in Figs. 10–12. Similar trends are observed as for the L_2 norm of φ_0 , however in most cases the decay

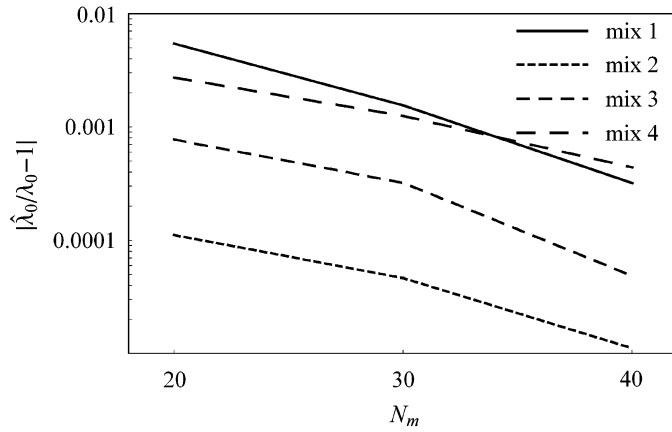


Fig. 10. Error between spectral method dominant strange eigenmode decay rate $\hat{\lambda}_0$ and reference $N_m = 50$ solution λ_0 for $Pe = 10^4$.

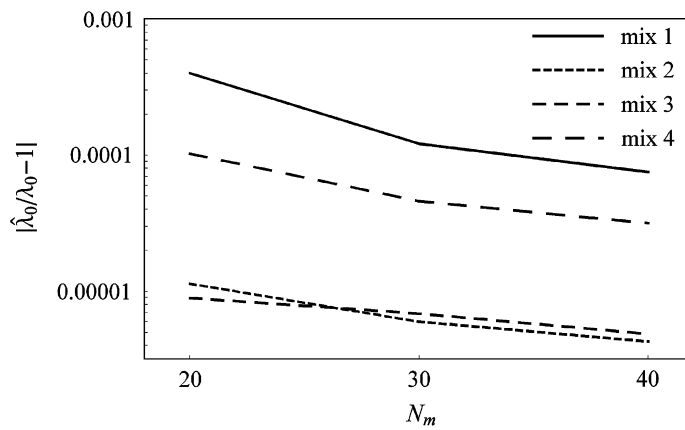


Fig. 11. Error between spectral method dominant strange eigenmode decay rate $\hat{\lambda}_0$ and reference $N_m = 50$ solution λ_0 for $Pe = 10^3$.

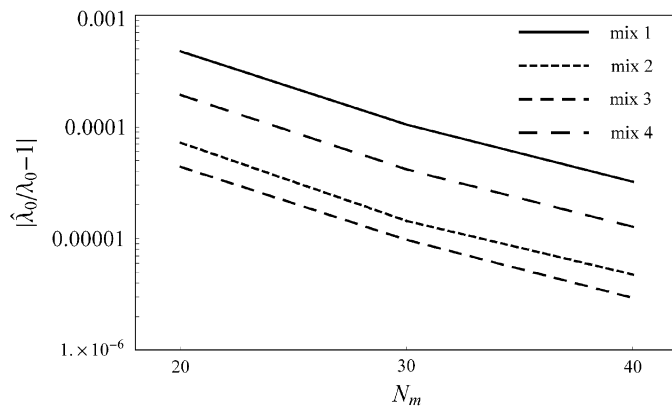


Fig. 12. Error between spectral method dominant strange eigenmode decay rate $\hat{\lambda}_0$ and reference $N_m = 50$ solution λ_0 for $Pe = 10^2$.

rate can be predicted to several orders of magnitude greater accuracy. Fig. 11 suggests that the spectral resolution $N_m = 20$ used to generate the values of λ_0 in Fig. 3 at $Pe = 10^3$ may be accurate to 0.1%. Accordingly, selection of an appropriate spectral resolution N_m (and hence N) for the composite spectral method depends on what information is wanted. For process optimization, accurate resolution of λ_0 may be all that is required, so solution of φ_0 is unnecessary and the computational burden can be significantly reduced.

6. Conclusions

The composite spectral method provides an efficient means of exploring solutions of the advection–diffusion equation over the associated control parameter space \mathcal{Q} , exhibiting the classic advantage of spectral accuracy (i.e. exponential convergence), and avoiding numerical diffusion associated with methods involving spatial discretization. The method provides approximate solutions to the ADE in the form of the problem’s natural persistent pattern, the so-called “strange eigenmodes”. The NPP’s form a complete set and are the natural modes of the system, independent of initial and boundary conditions and domain sources. Solution in terms of these modes is advantageous in that any solution for a specific initial condition may be reconstructed from the finite set of strange eigenmodes, and that all but the short-time ADE dynamics are governed solely by the leading strange eigenmodes, which may be determined in isolation at a reduced computational expense.

A temporally piecewise constant approximation of the advective velocity forms the kernel of the composite spectral method, facilitating subsequent construction of solutions to the ADE from solutions for each of the steady flows comprising the approximate flow. We show in Appendix C that accurate solutions to λ_k can be obtained with a small number of steady flows which comprise this approximation. Efficiency of the method stems from exploitation of the approximate form of, and symmetries between, the advective velocity fields over the control parameter space of the ADE. As the ADE is linear, and the approximated velocity field temporally piecewise constant, solutions for individual steady flows can be amalgamated to approximate the solution for a given unsteady flow. Flow symmetries facilitate further reduction in computation as mappings to construct classes of flows from an underlying subset can be applied at latter steps in the methodology. With minor modifications the method can also be applied to spatially periodic systems; in the context of chaotic advection relevant examples include any reoriented duct flow such as the Partitioned Pipe, Twisted Pipe, 3D Rotated Arc Mixer and many others. In general, the composite spectral method can be applied to any set of flows which reduce to a small set of topologically distinct fundamental flows, either in space or time. Using relevant symmetries, the transport properties over the complete set can be determined much more efficiently than by conventional methods, and the smaller the set of fundamental flows, the larger the computational gain.

Some examples of more complex flows with inherent symmetries are shown in Fig. 13. The 2D vortex array similar to that of Rothstein et al. [27] consists of an array of arbitrarily driven point vortices confined within a square cavity. As shown, there exist 10 (a - j) fundamental flows, from which the full set of 64 vortices can be mapped. For example, vortices e_1 , e_2 and e_3 are mapped via the rotation operator \mathbf{R}_1 , and e_4 , e_5 , e_6 , e_7 are mapped by a combination of this and the reflection operator \mathbf{R}_2 . Subsequently, the full flow field can be constructed via scaling and superposition.

Similar to the RAM, the partitioned pipe mixer flow [14] can be reoriented at certain times as shown. Temporal variation of the outer sleeve rotational velocity $\Omega_0(t)$ can be mapped by scaling, and reorientation subsequently mapped by the rotation operator \mathbf{R}_1 .

The vortex mixing flow [12] in the Stokes regime consists of three superimposed temporal flows arising from motion of the boundary elements $\Omega_0(t)$, $\Omega_1(t)$, $\Omega_2(t)$, where the latter flow can be mapped from the flow arising from $\Omega_1(t)$ via the reflection operator \mathbf{R}_1 . Temporal variation and combination of these flows is subsequently captured by scaling and superposition.

Attention in this paper has focussed on chaotic advection–diffusion systems as illustrative examples, however the method is applicable to any linear advection–diffusion problem, e.g. extension to incorporate linear reaction kinetics is straightforward. For single irreversible reactions of the form $\mathcal{A} + \mathcal{B} \rightarrow \mathcal{C}$, Chella and Ottino [2] show that if the reaction kinetics are fast with respect to advection and diffusion, the system can be expressed as an ADE (1), where ϕ represents the difference in concentration between species \mathcal{A} and \mathcal{B} . Like-

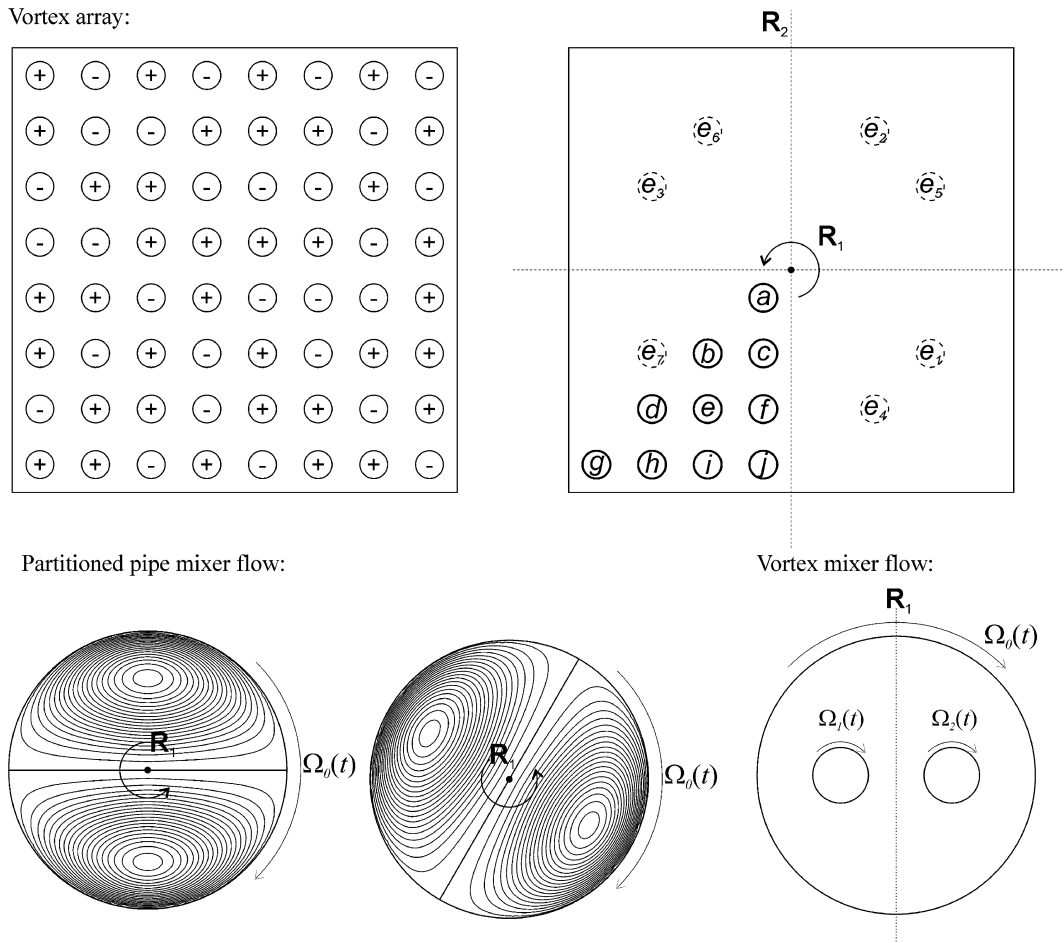


Fig. 13. Examples of flows with inherent symmetries.

wise, for instantaneous reaction or dissolution kinetics at a solid/fluid boundary, the system may also be modelled [13] via (1) with Dirichlet boundary conditions. Temporal periodicity of the advective velocity is not strictly necessary either; for aperiodic fields, analysis of the ADE can proceed over some finite time T as described in Section 2, however as this finite time may not correspond to the asymptotic limit, a larger number of strange eigenmodes may require resolution to characterise transport over T . Efficiency of the method in this case is limited by the computational expense of constructing \mathbf{S} which increases with T . It is also possible to consider problems involving with variable boundary condition types (e.g. heat transfer with some boundaries fixed heat flux, other fixed temperature), so long as the combinations of boundary condition distributions over \mathcal{Q} under consideration are finite. When the boundary condition type distribution is constant in time, then different type distributions can be simply considered as separate cases. If the boundary type distribution changes at times t_i^* but is otherwise piecewise steady, then the solution operator $\mathbf{S}(t)$ must be re-projected via $\mathbb{P}_{i,j}$ onto new basis functions in (4) to satisfy the evolving boundary conditions, and analysis can proceed as usual on the solution operator: $\mathbf{S}(T) = \mathbf{S}_1(t_1^*) \cdot \mathbb{P}_{1,2} \cdot \mathbf{S}_2(t_2^*) \cdots \mathbf{S}_k(t_k^*) \cdot \mathbb{P}_{k,1}$.

Although symmetry is naturally inherent to Stokesian flows and simple geometries as depicted in the examples above, the composite spectral method can be applied to complex flows and/or geometry. If the temporal flow field over a fixed yet possibly complex geometry can be decomposed (to desired resolution) into a set of steady basis modes, then study of scalar transport can be performed by application of the composite spectral method to this basis via scaling and superposition. As the transport problem is decoupled from the fluid mechanics, in principle the method can be applied to more complex flows such as granular, transition and turbulent flows, which may be determined analytically, numerically or experimentally; e.g. a non-Newtonian flow

is studied in Lester et al. [16]. In general, for nonlinear processes (i.e. inertial flows, non-Newtonian rheology, etc.), the set of flows over \mathcal{Q} cannot simply be reconstructed from a small set of basis flows by linear mappings such as scaling and superposition and furthermore flow symmetries inherently breakdown in the nonlinear regime. However, study of approximate scalar transport in a turbulent flow is possible by truncating higher wavenumber signals and employing an appropriate subgrid diffusion model, such that a modest set of base flows corresponding to spectral basis functions is required. In this case the compromise between the number of base flows and errors introduced by the subgrid diffusion model is quite limiting, and all of the flows over \mathcal{Q} must be determined.

Limitations of the method include application to nonlinear problems; in such cases multiple non-trivial attractors can exist within phase space and so asymptotic behaviour cannot easily be prescribed *a priori*. However, parametric study of transport dynamics in the absence of nonlinear processes still provides valuable insight into the global structure of scalar transport, and provides guidance for design and optimization with respect to the full nonlinear problem.

The majority of initial computation for the composite spectral method is the calculation of the spectral advection coefficients $\tilde{H}_{n,m}^i$, as is necessary for any spectral method. For large systems ($N \sim \mathcal{O}(10^5)$) solution of the nonsymmetric eigenproblem associated with calculation of the ADE strange eigenmodes becomes problematic, and represents the most immediate limitation to exploring large ($\gtrsim 10^7$) Peclet numbers, although this limitation applies to most numerical methods. For smaller systems (and low M), solution of the eigenproblem is relatively rapid, but must be applied to every point within the finite set \mathcal{Q} . As only this step need be repeated for each point, the relative efficiency of the method increases with the size of \mathcal{Q} .

Application of the composite spectral method to the ADE governing a 2D chaotic flow suggests the method is approximately 6000 times more efficient in approximating the dominant strange eigenmodes than a finite volume technique. Results from the method were also verified against high resolution CFD results, and the analysis suggests that the method exhibits spectral accuracy. These investigations establish the efficiency, accuracy and convergence of the composite spectral method and indicates it is a powerful technique for exploring quantitative and qualitative behaviours over the control parameter space of advection/diffusion systems.

Appendix A. Extension to inhomogeneous systems

Extension of the composite spectral method to inhomogeneous boundary conditions and/or non-zero source terms $f(\mathbf{x}, t)$ is straightforward. Linearity of the ADE facilitates decomposition into the pseudo-steady $\bar{\phi}$ and transient $\tilde{\phi}$ solutions: $\phi(\mathbf{x}, t) = \tilde{\phi}(\mathbf{x}, t) + \bar{\phi}(\mathbf{x}, t)$. The pseudo-steady solution $\bar{\phi}$ satisfies the Laplace equation over \mathcal{D} subject to the inhomogeneous boundary conditions

$$\nabla^2 \bar{\phi} = 0, \quad (\text{A.1})$$

$$\varrho \bar{\phi}|_{\partial \mathcal{D}} + (1 - \varrho) \nabla \bar{\phi} \cdot \mathbf{n}|_{\partial \mathcal{D}} = q(\mathbf{x}, t), \quad (\text{A.2})$$

and so may be solved analytically *a priori* using separation of variables and eigenfunction expansion to satisfy the boundary condition with t treated as an independent parameter. This decomposition yields homogeneous boundary conditions for $\tilde{\phi}$, and augments the source term and initial conditions as

$$\frac{\partial \tilde{\phi}}{\partial t} + \mathbf{v} \cdot \nabla \tilde{\phi} = \frac{1}{Pe} \nabla^2 \tilde{\phi} + F(\mathbf{x}, t), \quad (\text{A.3})$$

$$\tilde{\phi}(\mathbf{x}, 0) = \phi_0(\mathbf{x}) - \bar{\phi}(\mathbf{x}, 0), \quad (\text{A.4})$$

$$\varrho \tilde{\phi}|_{\partial \mathcal{D}} + (1 - \varrho) \nabla \tilde{\phi} \cdot \mathbf{n}|_{\partial \mathcal{D}} = 0, \quad (\text{A.5})$$

where $F(\mathbf{x}, t) = f(\mathbf{x}, t) - \frac{\partial \bar{\phi}}{\partial t} - \mathbf{v} \cdot \nabla \bar{\phi}$. Again spectral analysis is possible for $\tilde{\phi}$ based on an expansion in terms of the \mathcal{L}_1 eigenfunctions which satisfy the homogeneous boundary conditions (A.5): $\tilde{\phi}(\mathbf{x}, t) = \sum_n^\infty \tilde{\Phi}_n(t) \omega_n(\mathbf{x})$, yielding the linear inhomogeneous system of ODEs similar to (4):

$$\frac{d\tilde{\Phi}_n}{dt} = - \sum_{m=0}^\infty H_{n,m}(t) \tilde{\Phi}_m - \frac{\mu_n^2}{Pe} \tilde{\Phi}_n + \gamma_n(t), \quad (\text{A.6})$$

where $\gamma_n(t)$ is the source term spectral expansion coefficient:

$$\gamma_n(t) = \int_{\mathcal{D}} \omega_n(\mathbf{x}) F(\mathbf{x}, t) d\mathbf{x}. \quad (\text{A.7})$$

Truncation to N terms yields the finite system

$$\frac{d\tilde{\Phi}}{dt} = \mathbf{A}(t)\tilde{\Phi} + \mathbf{F}(t), \quad (\text{A.8})$$

where $\mathbf{F}(t)$ is the vector of $\gamma_n(t)$ terms, and $\tilde{\Phi}(t)$ may be expressed in terms of the homogeneous $\tilde{\Phi}_h(t)$ and particular $\tilde{\Phi}_p(t)$ solutions

$$\tilde{\Phi}(t) = \tilde{\Phi}_h(t) + \tilde{\Phi}_p(t) = \mathbf{S}(t)\mathbf{S}(0)^{-1}\tilde{\Phi}(0) + \mathbf{S}(t) \int_0^t \mathbf{S}(\tau)^{-1}\mathbf{F}(\tau)d\tau. \quad (\text{A.9})$$

Analysis of the homogeneous solution of $\tilde{\phi}$ is carried out in exactly the same fashion as for the homogeneous ADE (1): the strange eigenmodes in spectral space are approximated by the eigenvalues and eigenvectors of $\mathbf{S}(t)$, and the computational approach is the same. For the particular solution the source term $F(t)$ represents a continuous perturbation of the solution from the inertial manifold, and decay back to the manifold is governed by the strange eigenmodes.

These dynamics are illustrated by considering the impulse $\mathbf{F}(t) = \mathbf{F}_0\delta(t - t_0)$, where $\delta(t)$ represents the Dirac delta function. In this case, the particular solution is $H(t - t_0)\mathbf{S}(t)\mathbf{S}(t_0)^{-1}\mathbf{F}_0$ where $H(t)$ is the Heaviside step function, and so the impulse at time t_0 converges to the inertial manifold in the same manner as the strange eigenmodes for the initial condition $\tilde{\Phi}(0)$ in the homogeneous solution. In general, the source term may be expanded in terms of the strange eigenmodes

$$\mathbf{F}(t) \approx \sum_{k=0}^N \hat{F}_k(t) \mathbf{s}_k(t) e^{\hat{\lambda}_k t}. \quad (\text{A.10})$$

Hence from (A.9) the particular solution is

$$\tilde{\Phi}_p(t) \approx \sum_{k=0}^N \mathbf{s}_k(t) e^{\hat{\lambda}_k t} \int_0^t \hat{F}_k(\tau) d\tau, \quad (\text{A.11})$$

and the transient solution is approximated by

$$\tilde{\phi}(\mathbf{x}, t) \approx \sum_{k=0}^N \left(\hat{\alpha}_k + \int_0^t \hat{F}_k(\tau) d\tau \right) \hat{\phi}_k(\mathbf{x}, t) e^{\hat{\lambda}_k t}. \quad (\text{A.12})$$

Given approximation of the ADE strange eigenmodes, computation of the particular solution is relatively inexpensive so long as the eigenvectors $\mathbf{s}_k(t)$ for $t \in [0, T]$ are solved to high enough temporal resolution to allow accurate integration of $F_k(t)$ in (A.9). Note that although the strange eigenmodes are independent of $q(\mathbf{x}, t)$ and $f(\mathbf{x}, t)$, they are dependent upon the boundary coefficient q as both the \mathcal{L}_1 and \mathcal{L}_2 operator eigenfunctions must satisfy the homogeneous boundary conditions (A.5).

Appendix B. Composite mappings and flows derived for the lid-driven cavity

To illustrate the composite mapping method outlined in Section 3, we explore the well-known lid-driven cavity system. This Appendix is aimed to clarify the abstract exposition in the main body of the paper. The mappings for a Stokesian lid-driven cavity flow in the square domain $\{x, y\} = [0, 1] \times [0, 1]$ is depicted in Fig. B.1. Defining the fundamental flow $\tilde{\mathbf{v}}_1(\mathbf{x})$ as that associated with steady translation of the $y = 0$ boundary with unit velocity in the x -direction, generalisation to the case where all boundaries simultaneously and arbitrarily translate can be achieved by appropriate mappings of this fundamental flow.

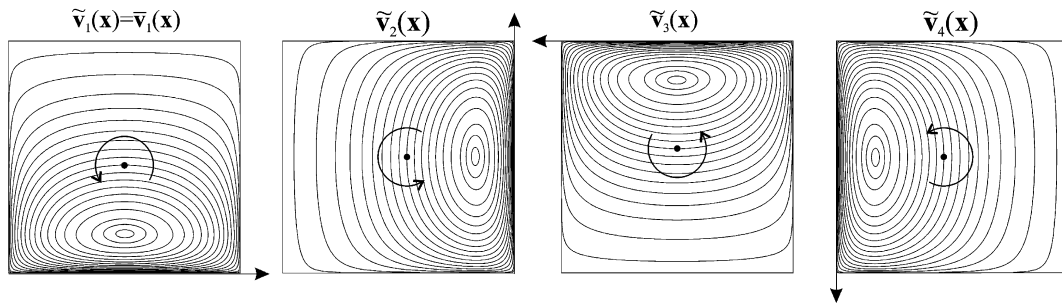
Flows arising from motion of the $x = 0$, $y = 1$ and $x = 1$ boundaries (denoted $\tilde{\mathbf{v}}_2(\mathbf{x})$, $\tilde{\mathbf{v}}_3(\mathbf{x})$, $\tilde{\mathbf{v}}_4(\mathbf{x})$ respectively) can be constructed by rotation of the fundamental flow $\tilde{\mathbf{v}}_1(\mathbf{x})$ around the point $\{1/2, 1/2\}$. Defining \mathcal{R}_i as the operator associated with rotation through angle $(i - 1)\pi/2$, the flows mapped by the rotation

operator are $\tilde{v}_i(\mathbf{x}) = \mathcal{R}_i[\tilde{v}_1(\mathbf{x})]$ for $i = 1:4$. As such, the single fundamental flow ($\bar{I} = 1$) is mapped by the rotation operator \mathcal{R} to form the set of 4 intermediate flows ($\bar{I} = 4$):

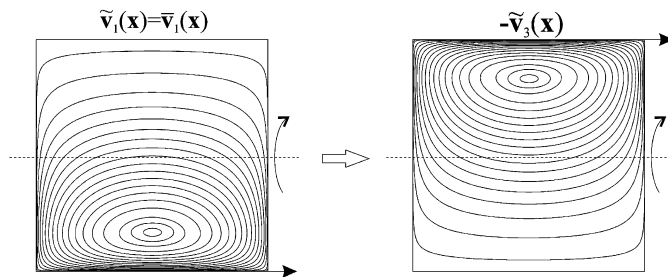
$$\{\tilde{v}_i(\mathbf{x})\} \xrightarrow{\mathcal{R}} \{\tilde{v}_i(\mathbf{x})\}.$$

The velocity field $\tilde{v}_3(\mathbf{x})$ arising from motion of the $y = 1$ boundary can also be constructed by reflection of the base flow $\tilde{v}_1(\mathbf{x})$ through the $y = 1/2$ axis, albeit reversed. In general the reflection operator yields flows which are distinct with respect to rotation, however symmetry of $\tilde{v}_1(\mathbf{x})$ along $x = 1/2$ in this case renders such mappings indistinct.

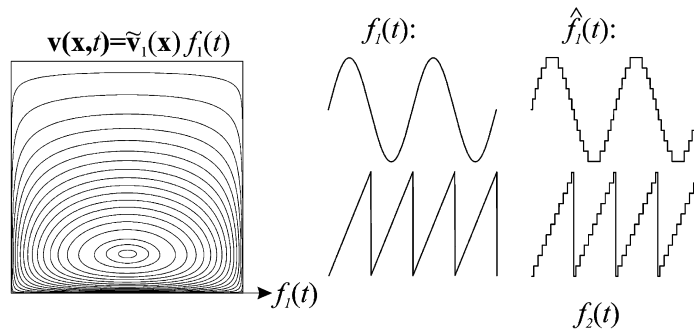
Rotation:



Reflection:



Scaling:



Superposition:

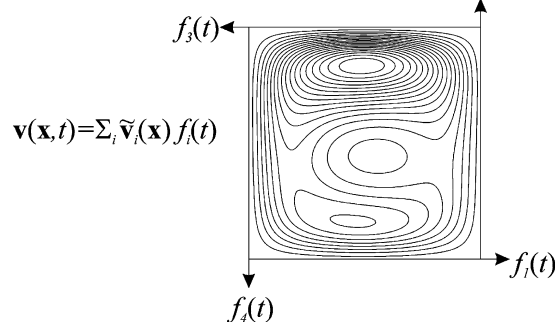


Fig. B.1. Rotation, reflection, scaling and superposition mappings for square cavity flow.

Via scaling, the fundamental flow $\bar{\mathbf{v}}_1(\mathbf{x}) = \tilde{\mathbf{v}}_1(\mathbf{x})$ can also be generalised to the case where the $y = 0$ boundary moves with bounded periodic velocity $\hat{f}_1(t) \in [f_{\min}, f_{\max}]$. Within the Stokes regime, the resultant unsteady velocity field $\mathbf{v}(\mathbf{x}, t)$ is simply a temporal scaling of the fundamental flow: $\mathbf{v}(\mathbf{x}, t) = \bar{\mathbf{v}}_1(\mathbf{x})\hat{f}_1(t)$. The forcing function $\hat{f}_1(t)$ can be approximated by the piecewise steady function $f_1(t) = \sum_i f_{1,i}h_i(t)$, comprising of the indicator function $h_i(t) = 0, 1$, and the I_{\max} discrete values of $f_{1,i}$ distributed over $[f_{\min}, f_{\max}]$. This approximation forms a basis for the piecewise steady approximate velocity field $\hat{\mathbf{v}}(\mathbf{x}, t) = \sum_i^I \mathbf{v}_i(\mathbf{x})h_i(t)$ in terms of the set of I_{\max} steady flows $\mathbf{v}_i(\mathbf{x}) = \tilde{\mathbf{v}}_1(\mathbf{x})f_{1,i}$. As such, these steady flows can be used to approximate any bounded forcing function $\hat{f}_1(t)$.

Using superposition, this concept can be extended to the case where all boundaries translate simultaneously with respective velocities $\hat{f}_i(t) \in [f_{\min}, f_{\max}]$; i.e. $\hat{\mathbf{v}}(\mathbf{x}, t) = \sum_i \tilde{\mathbf{v}}_i(\mathbf{x})\hat{f}_i(t)$. The piecewise steady approximation is likewise with \mathbf{v}, f , replacing $\hat{\mathbf{v}}, \hat{f}$. The scaling/superposition operator denoted \mathcal{S}_i maps all possible combinations of the reoriented flows

$$\mathbf{v}_i(\mathbf{x}) = \mathcal{S}_i[\tilde{\mathbf{v}}_1(\mathbf{x}), \dots, \tilde{\mathbf{v}}_I(\mathbf{x})] = \sum_j f_{j,i} \tilde{\mathbf{v}}_j(\mathbf{x}),$$

resulting in a set of $I = I_{\max}^4$ steady flows, each of which are characterised by the set of scalings $\{f_{1,i_1}, \dots, f_{4,i_4}\}$. In practice it is unlikely all of these combinations are required, however this mapping demonstrates the ability to approximate the velocity field for any arbitrary set of boundary velocities. The rotation/reflection and scaling/superposition mappings facilitate construction of the steady flows \mathbf{v}_i associated with simultaneous motion of all boundaries of the square lid-driven cavity from the single fundamental flow $\bar{\mathbf{v}}_1(\mathbf{x})$:

$$\{\bar{\mathbf{v}}_1(\mathbf{x})\} \xrightarrow{\mathcal{R}} \{\tilde{\mathbf{v}}_i(\mathbf{x})\} \xrightarrow{\mathcal{S}} \{\mathbf{v}_i(\mathbf{x})\}.$$

The resultant piecewise steady approximation is a composite of these steady flows: $\mathbf{v}(\mathbf{x}, t) = \sum_i^I \mathbf{v}_i(\mathbf{x})h_i(t)$, where $h_i(t)$ is now the indicator function for the set of scalings $\{f_{1,i_1}, \dots, f_{4,i_4}\}$ associated with \mathbf{v}_i . In this example application of the operators \mathcal{R}_i , \mathcal{S}_i is the reverse of (18), however this structure is still compatible with the general decomposition (16).

Appendix C. Operations count and accuracy

To quantify the efficiency of the method, we review the computational cost and accuracy of each step in the method outline. The mapping decomposition (17) admits a wide array of possible mapping protocols, and so the specific computational expense of the method can vary markedly. Moreover, the optimal storage and computation protocol varies significantly with the class of flows under consideration. As such, we consider the most general case involving all possible combinations of the N_{Pe} Peclét numbers and I component flows in (14), with the understanding that significant further computational reduction is more likely.

N_Q denotes the total number of distinct composite solutions $\mathbf{S}(T; \chi, Pe)$ in (25). These solutions are composed from (an average of) N_T selections from the set of N_S distinct (with respect to i , Pe or t) component solutions $\mathbf{S}_{i,Pe}(t)$. In turn, these solutions are mapped from the N_{\sim} distinct (with respect to j , Pe or t) intermediate solutions $\tilde{\mathbf{S}}_{j,Pe}(t)$, resolved in t to Δt where $\Delta t = T2^{-N_{\Delta t}}$. Accurate solution of $\tilde{\mathbf{S}}_{j,Pe}(t)$ requires consideration of the shorter time δt , where $\delta t = T2^{-N_{\delta t}}$, $N_{\delta t} \geq N_{\Delta t}$. We assume the scaling factors $s_{i,j}$ in (20) are evenly discretised as $s_{i,j} = j_i \Delta s_i$, and $j_i = -N_j : N_j$ for all i .

Steps 1 and 2 to classify the velocity fields over Q do not explicitly involve computation; rather, they tax the insight and judgement of the investigator. In Step 1 the piecewise steady velocity approximation (14) is defined, and error in the fundamental matrix solution can be quantified as follows. Let $\mathbf{A}(t)$ denote the piecewise steady approximation to the exact advection diffusion operator $\hat{\mathbf{A}}(t)$, where $\mathbf{A}(t) = \mathbf{A}_i$ for $t \in [t_{i-1}, t_i)$. The exact fundamental matrix solution is $\hat{\mathbf{S}}(t) = \exp(\Psi(t))$, where $\Psi(t)$ is given by the Magnus expansion [20]

$$\begin{aligned} \Psi(t) = & \int_0^t \hat{\mathbf{A}}(\tau_1) d\tau_1 - \frac{1}{2} \int_0^t \left[\int_0^{\tau_1} \hat{\mathbf{A}}(\tau_2) d\tau_2, \hat{\mathbf{A}}(\tau_1) \right] d\tau_1 + \frac{1}{4} \int_0^t \left[\int_0^{\tau_1} \left[\int_0^{\tau_2} \hat{\mathbf{A}}(\tau_3) d\tau_3, \hat{\mathbf{A}}(\tau_2) \right] d\tau_2, \hat{\mathbf{A}}(\tau_1) \right] d\tau_1 \\ & + \frac{1}{12} \int_0^t \left[\int_0^{\tau_1} \hat{\mathbf{A}}(\tau_2) d\tau_2, \left[\int_0^{\tau_1} \hat{\mathbf{A}}(\tau_3) d\tau_3, \hat{\mathbf{A}}(\tau_1) \right] \right] d\tau_1 + \dots, \end{aligned} \quad (\text{C.1})$$

and $[\mathbf{X}, \mathbf{Y}] = \mathbf{X} \cdot \mathbf{Y} - \mathbf{Y} \cdot \mathbf{X}$. The approximate solution over $t \in [0, t_1]$ is simply $\mathbf{S}_1(t) = \exp(\mathbf{A}_1 t)$, and we define the error $\epsilon_1(t) = \Psi(t) - \mathbf{A}_1 t$. The exact fundamental matrix $\hat{\mathbf{S}}(t)$ may be expanded via the Baker–Campbell–Hausdorff [4] formula as:

$$\begin{aligned} \hat{\mathbf{S}}(t) &= \exp(\mathbf{A}_1 t + \epsilon_1(t)) \\ &= \exp(\mathbf{A}_1 t) \cdot \exp(\epsilon_1(t)) \cdot \exp\left(\frac{1}{2}[\mathbf{A}_1 t, \epsilon_1(t)]\right) \cdot \exp\left(\frac{1}{12}[\mathbf{A}_1 t, [\mathbf{A}_1 t, \epsilon_1(t)]]\right) \\ &\quad \cdot \exp\left(-\frac{1}{12}[\epsilon_1(t), [\mathbf{A}_1 t, \epsilon_1(t)]]\right) \cdot \exp\left(-\frac{1}{48}[\epsilon_1(t), [\mathbf{A}_1 t, [\mathbf{A}_1 t, \epsilon_1(t)]]]\right) \\ &\quad \cdot \exp\left(-\frac{1}{48}[\mathbf{A}_1 t, [\epsilon_1(t), [\mathbf{A}_1 t, \epsilon_1(t)]]]\right) \cdots \\ &= \exp(\mathbf{A}_1 t) \cdot \Lambda_1(t), = \mathbf{S}_1(t) \cdot \Lambda_1(t). \end{aligned} \tag{C.2}$$

Hence, $\Lambda_1(t)$ is the relative error for approximating $\mathbf{A}_1 \approx \hat{\mathbf{A}}(t)$ over $t \in [0, t_1]$. This result extends to all $t \in [0, T]$ as

$$\hat{\mathbf{S}}(t) = \prod_i^n \mathbf{S}_i(t_i - t_{i-1}) \cdot \Lambda_i(t_i - t_{i-1}), \tag{C.3}$$

quantifying how the errors $\hat{\mathbf{v}} - \mathbf{v}$ (which decrease with N_j) propagate to the fundamental matrix $\mathbf{S}(t)$. These results provide guidance for appropriate approximation of \mathbf{v} in Eq. (14), such that accuracy is offset against the cost of increased computation. Eqs. (C.1) and (C.2) also provide a basis for extension of the method to higher order ($n > 0$) temporal approximation of \mathbf{v} where required.

Errors in the strange eigenmode decay rates λ_k arising from the piecewise steady approximation (14) can be determined by considering the following method for approximating the exact fluid velocity $\hat{\mathbf{v}}$. The steady flows \mathbf{v}_i which comprise \mathbf{v} can be specified by setting δv in the constraint $\|\hat{\mathbf{v}} - \mathbf{v}\|/\|\mathbf{v}\| \leq \delta v$. As such, δv represents the maximum possible relative error associated with the approximation \mathbf{v} . In the case of scaling of base flows, i.e. $\hat{\mathbf{v}}(\mathbf{x}, t) = \hat{f}(t)\mathbf{V}_0(\mathbf{x})$ (e.g. Section 4), then if \hat{f} ranges over $[f_{\min}, f_{\max}]$ and I_{\max} appropriately distributed values f_i are used to approximate \hat{f} , then $\delta v \approx 1/2I_{\max}$.

An upper bound for errors in λ_k can be derived by considering the worst-case scenario where $\mathbf{v} = (1 + \delta v)\hat{\mathbf{v}}$ over all T , hence $\hat{\mathbf{v}}$ is also piecewise steady. Denoting $\hat{\mathbf{H}}(t)$ as the exact spectral advection operator associated with $\hat{\mathbf{v}}$, then $\mathbf{S}(t) = \exp\{(1 + \delta v)\hat{\mathbf{H}}(t) + \frac{t}{\rho_e}\mathbf{D}\}$. In comparison, eigenvalues of the less accurate operator $\exp\{(1 + \delta v)(\hat{\mathbf{H}}(t) + \frac{t}{\rho_e}\mathbf{D})\}$ by scaling are exactly $1 + \delta v$ times greater than those of the exact solution. As such, δv represents an upper bound for errors in the strange eigenmode decay rates λ_k derived from the approximate piecewise steady velocity field \mathbf{v} . For a modest number of flows $I_{\max} = 10$, this upper bound is 5%, however in practice such errors are an order of magnitude lower.

Step 3 involves two distinct sources of error associated with spectral expansion of the ADE (4). The first error involves truncation of the resultant system to a finite (N) number of spectral modes, but no computation is undertaken. As N controls most of the compromise between accuracy and computational overhead of the method, Section 5 studies this in detail. As the method is purely spectral, spectral convergence is expected: i.e. the truncation error approaches zero faster than $\exp(-N^2 t)$ [9].

Second is the computational error associated with spectral expansion of the advective operator $\hat{\mathbf{v}} \cdot \nabla$ for each of the \bar{I} base flows, involving calculation of $\frac{1}{2}N^2$ integrals. (Expansion of the diffusion operator is analytic because the spectral basis functions are the Laplacian eigenfunctions.) Computation of these integrals (the coefficients $H_{n,m}$ in (6)) is normally expensive as the basis functions ω_n are highly oscillatory for large n . However, as the ω_n are orthogonal, they satisfy recurrence relations upon differentiation. As such, Levin’s [18] very efficient method can accurately (relative error $\sim \mathcal{O}(10^{-9})$) compute definite integrals of the form

$$\int_a^b Q_n(x)P(x)dx, \tag{C.4}$$

where $Q_n(x)$ is oscillatory with a differentiation recurrence. $P(x)$ is related to $\hat{\mathbf{v}}$ and minimally evaluated, so the method suitable for flow fields obtained numerically or experimentally. Although efficient, evaluation of (C.4) $\frac{1}{2}N^2 \times \bar{I}$ times is a significant computational overhead.

Step 4 involves calculation of the short time (δt) order N matrix exponentials ($\bar{\mathbf{h}}_i$ in (D.3)) for each of the \bar{I} fundamental flows. The Taylor series expansion is accurate to $\mathcal{O}(\delta t^5)$, and involves $3 \times \bar{I}$ order N matrix multiplications in total.

Step 5 involves application of the augmented scaling/superposition operator for each of the \bar{I} intermediate flows. If each $\bar{\mathbf{h}}_i^j$ for all j_i in (D.3) needs to be calculated, then \bar{I} order N matrix inversions and $2(N_j - 1) \times \bar{I}$ matrix multiplications are required. From these, the short time matrix solution $\tilde{\mathbf{S}}_{j,Pe}(\delta t)$ can be constructed via (D.3) for each of the \bar{I} intermediate flows for $\bar{I} \times \bar{I} + (N_{Pe} - 1)$ order N matrix multiplications.

Determination of $\tilde{\mathbf{S}}_{j,Pe}(\delta t 2^n)$ for $n = 1:N_{\delta t}$ via (D.5) needs $\bar{I} \times N_{Pe} \times N_{\delta t}$ order N matrix multiplications and additions. From these results, the matrix solution $\tilde{\mathbf{S}}_{j,Pe}(t)$ for any time $t \in [0, T]$ can be composed using Eq. (D.6). Using (D.3) directly, the errors in $\tilde{\mathbf{S}}_{j,Pe}(T)$ scale as $2^{-N_{\delta t}}$, whereas for (D.4) the errors scale as $2^{-5N_{\delta t}}$ for small $N_{\delta t}$ and limit toward $2^{-N_{\delta t}}$ with increasing $N_{\delta t}$.

The total possible number of distinct (with respect to i, Pe, t) component solutions $\mathbf{S}_{i,Pe}(t)$ is very large ($N_{Pe} \times I \times 2^{N_{At}}$), resulting in a huge number of possible permutations ($N_{Pe} \times I^{(2^{N_{At}})}$) for $\mathbf{S}(T; \chi, Pe)$ in (25), each corresponding to a distinct point within \mathcal{Q} . Although this blowup demonstrates the ability of the method to consider a very large number of points within \mathcal{Q} via the mapping (17), it is more relevant to consider much smaller numbers $N_{\tilde{\mathbf{S}}}$, $N_{\mathbf{S}}$ respectively of the distinct solutions $\tilde{\mathbf{S}}_{j,Pe}(t)$, $\mathbf{S}_{i,Pe}(t)$ from which $\mathbf{S}(T; \chi, Pe)$ are composed.

Computation of $\tilde{\mathbf{S}}_{j,Pe}(t)$ to resolution Δt is described by (D.6), with $n = 1 + N_{At} - N_{\delta t}$ replacing $n = 1$. As such, there are N_{At} terms in (D.6), however as $I_n = 0$ or 1 with equal probability, on average construction of all the $N_{\tilde{\mathbf{S}}}$ distinct component solutions $\tilde{\mathbf{S}}_{j,Pe}(t)$ involves a total of $N_{\tilde{\mathbf{S}}} \times \frac{1}{2} N_{At}$ order N matrix multiplications.

Step 6 involves calculation of the $N_{\mathbf{S}}$ distinct component solutions $\mathbf{S}_{i,Pe}(t)$ in (24) from the $N_{\tilde{\mathbf{S}}}$ distinct intermediate solutions $\tilde{\mathbf{S}}_{j,Pe}(t)$. This operation involves $2(N_{\mathbf{S}} - N_{\tilde{\mathbf{S}}})$ order N matrix multiplications.

Step 7 involves construction of the composite fundamental matrix solution $\mathbf{S}(T; \chi, Pe)$ for each of the $N_{\mathcal{Q}}$ points in \mathcal{Q} . As such, the computational overhead involves $N_{\mathcal{Q}} \times N_T$ order N matrix multiplications.

Step 8 involves solution of the leading M eigenvalues and eigenvectors of the order N unsymmetric matrix $\mathbf{S}(T; \chi, Pe)$ for each point in \mathcal{Q} . For M small ($\mathcal{O}(1)$) and $N \sim \mathcal{O}(10^5)$ the Arnoldi method is applicable, however as N increases further the problem becomes intractable for dense systems [8]. Conversely, if all the NPPs are required (i.e. $M = N$), then the QZ algorithm is more efficient; however, N is limited to $\mathcal{O}(10^4)$ for dense systems. Because computational cost increases steeply with N and M , these numerical limitations place practical upper bounds on both the Peclet number and number of NPPs that can be resolved by the composite spectral method.

The computational expense of the composite spectral method is summarised in Table C.1, for the most general case involving all possible combinations of mappings. Although the method appears to be computationally intensive, in many cases further computational savings arise due to omission or reduction of particular steps, and often \bar{I} , \tilde{I} , N_{Pe} are small.

Table C.1
Summary of computational expenses of the composite spectral method

Step	Calculation	Computation
3	$H_{n,m}$ in $\bar{\mathbf{H}}_i$ for $i = 1 : \bar{I}$	$\bar{I} \times \frac{1}{2} N^2$ integrals
4	$\exp(\bar{\mathbf{H}}_i \delta t)$ for $i = 1 : \bar{I}$	$3\bar{I}$ mm's
5a	$\bar{\mathbf{h}}_i^j$ for all $i = 1 : \bar{I}$, $j_i = -N_j:N_j$	\bar{I} mi's & $\bar{I} \times 2(N_j - 1)$ mm's
5b	$\tilde{\mathbf{S}}_{j,Pe}(\delta t)$ for $i = 1 : \bar{I}$	$\tilde{I} \times \bar{I} + (N_{Pe} - 1)$ mm's
5c	$\tilde{\mathbf{S}}_{j,Pe}(\delta t 2^n)$ for $i = 1 : \tilde{I}$, $n = 1:N_{\delta t}$	$\tilde{I} \times N_{Pe} \times (N_{\delta t} - 1)$ mm's
5d	$N_{\tilde{\mathbf{S}}} \times \tilde{\mathbf{S}}_{j,Pe}(t)$ to resolution Δt	$N_{\tilde{\mathbf{S}}} \times \frac{1}{2} N_{At}$ mm's
6	$N_{\mathbf{S}} \times \mathbf{S}_{i,Pe}(t)$ to resolution Δt	$2(N_{\mathbf{S}} - N_{\tilde{\mathbf{S}}})$ mm's
7	$N_{\mathcal{Q}} \times \mathbf{S}(T; \chi, Pe)$	$N_{\mathcal{Q}} \times N_T$ mm's
8	$N_{\mathcal{Q}}$ strange eigenmodes	$N_{\mathcal{Q}} \times (N, M)$ ep's

mm = order N matrix multiplication, mi = order N matrix inversion, (N, M) ep = solution of leading M eigenvectors and eigenvalues of order N unsymmetric matrix.

Appendix D. Efficient calculation of exponentials of matrix sums

Following Eqs. (22) and (23), we require an efficient method to calculate matrix exponentials which arise from application of the scaling/superposition operator

$$\begin{aligned} \tilde{\mathbf{S}}_{j,Pe}(t) &= \exp \left\{ \left(\tilde{\mathbf{H}}_j - \frac{1}{Pe} \mathbf{D} \right) t \right\}, \\ &= \exp \left\{ \left(\sum_i^{\bar{I}} s_{i,j} \bar{\mathbf{H}}_i - \frac{1}{Pe} \mathbf{D} \right) t \right\}, \end{aligned} \tag{D.1}$$

for different values of the variables $s_{i,j}$, Pe and all $t \in [0, T]$. Often the scaling factors $s_{i,j}$ are evenly discretized due to the piecewise steady approximation (14), and so may be expressed as $s_{i,j} = j_i \Delta s_i$, where j_i are integers.

We summarise efficient calculation of exponentials of the form $\exp(\sum_i j_i \mathbf{M}_i t)$ as follows. For exponentials involving sums of non-commuting matrices, errors in the product expansion $\exp(\sum_i j_i \mathbf{M}_i t) \approx \prod_i \exp(\mathbf{M}_i t)^{j_i}$ can be large as they scale as t^{2j_i} , and these results need to be calculated for all $t \in [0, T]$. However, when calculating the single exponential $\exp(\mathbf{M} t)$, a Taylor series expansion performed for small times δt is most efficient [34], and the results subsequently scaled up to T via matrix multiplication. Returning to the matrix sum, if the product expansion above is performed *prior* to scaling, these errors now scale as δt^{2j_i} , and so this expansion can be applied accurately with no extra computational expense. For different sets $\{j_i\}$ involving increasing j_i , the product expansion can be “built up” by appropriate multiplication of additional terms $\exp(\mathbf{M}_i \delta t)$ prior to scaling. Finally, the exponential for any $t \in [0, T]$ to resolution δt can be constructed from the intermediate scalings between δt and T .

Specifically, the component exponentials in the product expansion can be efficiently calculated via the Taylor series expansion

$$\exp(\mathbf{M}) = \mathbf{I} + \mathbf{M} + \frac{\mathbf{M} \cdot \mathbf{M}}{2} \left(\mathbf{I} + \frac{\mathbf{M}}{3} + \frac{\mathbf{M} \cdot \mathbf{M}}{12} \right) + \mathcal{O}(\mathbf{M}^5). \tag{D.2}$$

Step 4 of the method requires calculation of the terms $\bar{\mathbf{h}}_i = \exp(\Delta s_i \bar{\mathbf{H}}_i \delta t)$ from (D.1) for all $i = 1 : \bar{I}$, which can be efficiently achieved via (D.2), where $\delta t = T 2^{-N_{\delta t}}$, $N_{\delta t}$ a positive integer. Using these results, the short time matrix solution is constructed as

$$\tilde{\mathbf{S}}_{j,Pe}(\delta t) = \mathbf{d} \cdot \prod_i^{\bar{I}} \bar{\mathbf{h}}_i^{j_i} + \mathcal{O} \left(\sum_i^{\bar{I}} (\Delta s_i \delta t)^{2j_i} \right), \tag{D.3}$$

where $\mathbf{d} = \exp(-\frac{\delta t}{Pe} \mathbf{D})$ is analytic for all Pe . In the case of $\bar{I} = 1$, the fourth-order hybrid approximation of Suzuki [31] is more accurate

$$\begin{aligned} \exp(m\mathbf{M}_1 + m\mathbf{M}_2) &= \exp \left(\frac{m^3}{144} [\mathbf{M}_2, [\mathbf{M}_1, \mathbf{M}_2]] \right) \cdot \exp \left(\frac{m}{6} \mathbf{M}_2 \right) \cdot \exp \left(\frac{m}{2} \mathbf{M}_1 \right) \exp \left(\frac{2m}{3} \mathbf{M}_2 \right) \\ &\cdot \exp \left(\frac{m}{2} \mathbf{M}_1 \right) \cdot \exp \left(\frac{m}{6} \mathbf{M}_2 \right) \cdot \exp \left(\frac{m^3}{144} [\mathbf{M}_2, [\mathbf{M}_1, \mathbf{M}_2]] \right) + \mathcal{O}(m^5), \end{aligned} \tag{D.4}$$

which can also be applied iteratively for small \bar{I} . In this case, the component exponentials in (D.4) are still efficiently calculated via (D.2), and the product expansion (D.3) is modified in a manner consistent with (D.4). In essence, Eqs. (D.2) and (D.3) are the augmented scaling/superposition operator \mathcal{S}_j^\star . The high accuracy (up to $\mathcal{O}(\delta t^{5j_i})$ for (D.4)) of these formulae arise from the smallness of δt , but these results must be scaled up to any value of $t \in [0, T]$. Such arbitrary scaling can be achieved efficiently using the precise integration method of Zhong [34] which avoids the rounding errors that plague many such methods [7]:

$$\begin{aligned} \widehat{\mathbf{S}}_n &\equiv \tilde{\mathbf{S}}_{j,Pe}(\delta t 2^n) - \mathbf{I}, \\ \widehat{\mathbf{S}}_{n+1} &= 2\widehat{\mathbf{S}}_n + \widehat{\mathbf{S}}_n \cdot \widehat{\mathbf{S}}_n \quad \text{for } n = 0 : N_{\delta t} - 1. \end{aligned} \tag{D.5}$$

Finally, the exponential for any time $t \in [0, T]$ to resolution δt can be calculated as

$$\tilde{\mathbf{S}}_{j,Pe}(t) = \prod_{\substack{n=1 \\ I_n=1}}^{N_{\delta t}} \tilde{\mathbf{S}}_{j,Pe}(\delta t 2^n), \quad (\text{D.6})$$

where I_n is the n th digit from the right of $[\frac{t}{\delta t}]$ in binary form. Due to the wide variety of possible mapping combinations, it is not possible to prescribe optimal storage protocols for computation of the matrix exponential (D.1) for differing $\{s_{i,j}\}$. In most cases it is preferential to compute and store \mathbf{h}_i for $i = 1 : \bar{I}$, but the question of the best quantities to store in the hierarchy $\mathbf{h}_i \rightarrow \mathbf{h}_i^i \rightarrow \tilde{\mathbf{S}}_{j,Pe}(\delta t) \rightarrow \tilde{\mathbf{S}}_{j,Pe}(\delta t 2^n) \rightarrow \tilde{\mathbf{S}}_{j,Pe}(t)$ depends strongly on the specific nature of the flows \mathbf{v} in \mathcal{Q} . In the case of scaling only, Eq. (D.4) is simplified because \mathbf{D} is diagonal. For cases involving no scaling or superposition (i.e. t only in (D.1) is varied), the matrix exponential is best calculated directly via (D.2) and (D.5).

Appendix E. Supplementary data

Supplementary data associated with this article can be found, in the online version, at [doi:10.1016/j.jcp.2007.10.015](https://doi.org/10.1016/j.jcp.2007.10.015).

References

- [1] A. Adrover, S. Cerbelli, M. Giona, A spectral approach to reaction/diffusion kinetics in chaotic flows, *Computers and Chemical Engineering* 26 (2002) 125–139.
- [2] R. Chella, J.M. Ottino, Conversion and selectivity modifications due to mixing in unpremixed reactors, *Chemical Engineering Science* 39 (1984) 551–567.
- [3] V. Ganesan, M.D. Bryden, H. Brenner, Chaotic heat transfer enhancement in rotating annular flow systems, *Physics of Fluids* 9 (5) (1997) 1296–1306.
- [4] R. Gilmore, Baker–Campbell–Hausdorff formulas, *Journal of Mathematical Physics* (15) (1974) 2090–2092.
- [5] M. Giona, S. Ceribelli, V. Vitacolonna, Universality and imaginary potentials in advection–diffusion equations in closed flows, *Journal of Fluid Mechanics* 513 (2004) 221–237.
- [6] J.A. Glazier, A. Libchaber, Quasi-periodicity and dynamical systems: an experimentalists view, *IEEE Transactions on Circuits and Systems* 35 (7) (1988) 790–809.
- [7] G.H. Golub, C.F. Van Loan, *Matrix Computations*, Johns Hopkins University Press, Baltimore, MD, USA, 1991.
- [8] G.H. Golub, H.A. van der Vorst, Eigenvalue computation in the 20th century, *Journal of Computational and Applied Mathematics* 123 (2000) 35–65.
- [9] D. Gottlieb, S.A. Orszag, *Numerical Analysis of Spectral Methods: Theory and Applications*, Society for Industrial and Applied Mathematics, Philadelphia, PA, USA, 1977.
- [10] P.H. Haynes, J. Vanneste, What controls the decays of passive scalars in smooth flows? *Physics of Fluids* 17 (9) (2005) 097103–1–097103-16.
- [11] T.-Y. Hwu, D.-L. Young, Y.-Y. Chen, Chaotic advections for stokes flow in circular cavity, *Journal of Engineering Mechanics* 123 (8) (1997) 774–782.
- [12] S.C. Jana, G. Metcalfe, J.M. Ottino, Experimental and computational studies of mixing in complex stokes flows: the vortex mixing flow and multicellular cavity flows, *Journal of Fluid Mechanics* 269 (1994) 199–246.
- [13] J.D. Kirtland, G.J. McGraw, A.D. Stroock, Mass transfer to relative boundaries from steady three-dimensional flows in microchannels, *Physics of Fluids* 18 (2006) 073602-1–073602-13.
- [14] H.A. Kusch, J.M. Ottino, Experiments on mixing in continuous flows, *Journal of Fluid Mechanics* 236 (1992) 319–348.
- [15] A. Lefèvre, J.P.B. Mota, A.J.S. Rodrigo, E. Saatjian, Chaotic advection and heat transfer enhancement in Stokes flow, *International Journal of Heat and Fluid Flow* 24 (2003) 310–321.
- [16] D.R. Lester, G. Metcalfe, M. Rudman, Low Reynolds number scalar transport enhancement in viscous and non-Newtonian fluids, *International Journal of Heat and Mass Transfer*, submitted for publication.
- [17] D.R. Lester, G. Metcalfe, M. Rudman, Complete parametric solutions of scalar transport, *Physics Review Letters*, submitted for publication.
- [18] D. Levin, Fast integration of rapidly oscillatory functions, *Journal of Computational and Applied Mathematics* 67 (1996) 95–101.
- [19] W. Liu, G. Haller, Strange eigenmodes and decay of variance in the mixing of diffusive tracers, *Physica D* 188 (2004) 1–39.
- [20] W. Magnus, On the exponential solution of differential equations for a linear operator, *Communications in Pure and Applied Mathematics* (7) (1954) 649–654.
- [21] G. Metcalfe, M. Rudman, A. Brydon, L.J.W. Graham, R. Hamilton, Composing chaos: An experimental and numerical study of an open duct mixing flow, *AIChE Journal* 52 (2006) 9–28.

- [22] S.D. Müller, I. Mezić, J.H. Walthier, P. Koumoutsakos, Transverse momentum micromixer optimization with evolution strategies, *Computers and Fluids* 33 (2004) 521–531.
- [23] J.M. Ottino, *The Kinematics of Mixing: Stretching, Chaos and Transport*, Cambridge University Press, Cambridge, 1989.
- [24] J.M. Ottino, G. Metcalfe, S.C. Jana, Experimental studies of chaotic mixing, in: W. Ditto, L. Pecora, M. Shlesinger, M. Spano, S. Vohra, (Eds.), *Proceedings of the Second Experimental Chaos Conference*, Office of Naval Research, 1995.
- [25] R.T. Pierrehumbert, Tracer microstructure in the large-eddy dominated regime, *Chaos, Solitons and Fractals* 4 (6) (1994) 1091–1110.
- [26] A.J.S. Rodrigo, J.P.B. Mota, A. Lefèvre, E. Saadjin, On the optimization of mixing protocol in a certain class of three-dimensional Stokes flows, *Physics of Fluids* 15 (6) (2003) 1505–1516.
- [27] D. Rothstein, E. Henry, J.P. Gollub, Persistent patterns in transient chaotic fluid mixing, *Nature* 401 (1999) 770–772.
- [28] E. Saadjin, N. Midoux, M.I. Gastou Chassiang, J.C. Leprevost, J.C. André, Chaotic mixing and heat transfer between confocal ellipses: experimental and numerical results, *Physics of Fluids* 8 (3) (1996) 677–691.
- [29] M. Speetjens, G. Metcalfe, M. Rudman, Topological mixing study of non-Newtonian duct flows, *Physics of Fluids* (1999).
- [30] A.D. Stroock, G.J. McGraw, Investigation of the staggered herringbone mixer with a simple analytical model, in: J.M. Ottino, S. Wiggins, (Eds.), *Transport and mixing at the microscale*, *Philosophical Transactions of The Royal Society of London*, 2004.
- [31] M. Suzuki, Hybrid Exponential product formulas for unbounded operators with possible applications to Monte Carlo simulations, *Physics Letters A* 201 (5) (1995) 425–428.
- [32] T. Tel, A. de Moura, C. Grebogi, G. Károlyi, Chemical and biological activity in open flows: a dynamical system approach, *Physics Reports* 413 (2005) 191–196.
- [33] V. Toussaint, P. Carrière, J. Scott, J.-N. Gence, Spectral decay of a passive scalar in chaotic mixing, *Physics of Fluids* 12 (11) (2000) 2834–2844.
- [34] W.-X. Zhong, On precise integration method, *Journal of Computational and Applied Mathematics* 163 (2004) 59–78.